Subvolcanic magma pathways in transtensional regimes; AMS and structural evidence from SE Iceland

Vincent Twomey[1], William McCarthy[1]†, Craig Magee[2], Ben Latimer[1]

1 School of Earth & Environmental Sciences, University of St Andrews, St Andrews, UK, KY16 9AL

2 School of Earth and Environment, University of Leeds, Leeds, UK, LS2 9JT

† Corresponding author: wm37@st-andrews.ac.uk

Abstract

This study presents an integrated analysis of magmatic and tectonic strain data recorded within and around the Reyðarártindur intrusion, southeast Iceland, combining anisotropy of magnetic susceptibility (AMS) with UAV-based fracture mapping. Thermomagnetic experiments and petrography confirm AMS fabrics capture magmatic-state strain, defining a consistent NNE–SSW magnetic lineation with predominantly sub-horizontal orientations that is here interpreted to record lateral SSW magma flow during emplacement. Localised steep fabrics at intrusion margins and within inclined sheets indicate vertical magma transfer into fracture-controlled conduits during syn- to late-stage evacuation. UAV-derived structural data reveal a network of brittle fractures in the basaltic host rocks forming a left-stepping sigmoidal pattern, consistent with a sinistral Riedel shear system. This fracture architecture closely matches regional palaeostress orientations for southeast Iceland, indicating that the host rocks preserve the contemporaneous tectonic strain field.

Integration of these datasets demonstrates a spatial and kinematic correspondence between internal magmatic fabrics and external brittle structures: the dominant AMS fabric parallels the principal Riedel shear fracture set, indicating regional tectonic strain guided magma transport pathways. Fracture networks also acted as conduits for vertical magma migration, linking lateral flow within the intrusion to eruption-feeding sheets.

Our results demonstrate that magma flow in the Reyðarártindur intrusion was strongly influenced by the interaction between internal magmatic processes and the surrounding regional structures;that may have been kinematically governed by an active Riedel shear system, linking subvolcanic transport directly to tectonic strain. Our findings demonstrate how integrating magnetic fabrics with field relationships reveal the interplay between tectonics and subvolcanic magma transport mechanisms.

Keywords

Magma Emplacement; Tectonics; Reyðarártindur intrusion; SE Iceland; Fracture Analysis; Magnetic Fabrics; AMS.

Introduction

Magma migration, emplacement, and evacuation in the upper crust is influenced by the interplay of local and tectonic stresses, host rock rheology, and/or evolving magmatic conditions (e.g., Jacques and Reavy, 1994; Gudmundsson, 2011; Molina Garza et al., 2021; Memeti et al., 2022; Witcher et al., 2024; Koopmans et al., 2025). Unravelling how these interacting parameters dictate siting of intrusions and subsequent eruptions is an increasingly important societal challenge from both an energy supply and hazard mitigation perspective (e.g., Marti et al., 2016; Acocella et al., 2018; Magee et al., 2018; Mattsson et al., 2018). It has long been recognised that the architecture of sheet intrusions and plutons, from their chemistry and microstructure to external geometry, preserve evidence of the processes and interactions controlling their emplacement style and subsequent eruptive behaviour (e.g., Pollard and Johnson, 1973; Rubin, 1995; Rivalta et al., 2015; Brune et al., 2023). Traditional models of upper crustal magma emplacement include cauldron subsidence (Clough et al., 1909; Richey, 1927), diapirism (Marzec, 1927; Ramberg, 1970), and stoping (Daly, 1903), with the subsequent recognition of other processes such as laccolithic emplacement (Daly, 1933), ballooning (Cloos, 1926), and emplacement within tectonic structures (Hutton, 1982, 1988). However, competing emplacement models persist in many instances where available data are not mutually exclusive to one model (c.f., Vernon and Paterson, 1993; Paterson and Vernon, 1995; Molyneux and Hutton, 2000; McCarthy et al., 2015).

The integration of multiple datasets examining the interior of intrusions provides new insight on the complex history of their construction, resulting in the reinterpretation of many archetypal bodies of traditional emplacement models (e.g., O'Driscoll et al., 2006; Stevenson et al., 2007; McCarthy et al., 2015). For example, rock fabric analysis via magnetic methods, such as anisotropy of magnetic susceptibility (AMS), is established as a key tool in unlocking the internal strain archive within intrusions, particularly in the absence of visible petrofabrics (e.g., Bouchez, 1997; Borradaile and Jackson, 2010). The sensitivity of magnetic fabrics allows measurement of successive events during and post-crystallisation, shown to reflect internal magmatic processes, such as the piecemeal growth of laccoliths (e.g., Stevenson et al., 2007b; Magee et al., 2012; McCarthy et al., 2015). Magnetic fabrics have also been shown at the intrusion-host rock interface to record pure shear flattening arising from magma overpressure, consistent with adjacent host rock deformation (e.g., McCarthy et al., 2015; Köpping et al., 2023; Mattsson et al., 2024) and subsequent residual magma remobilisation during cooling (e.g., Jones et al., 2025; Williams et al., 2025). Conversely, in the presence of an external tectonic stress regime, magnetic fabrics demonstrated a unique ability to be sensitive to tectonic overprinting of precursor fabrics throughout crystallisation (e.g., Latimer et al., 2024), extending beyond classic studies that rely on enclave geometry to determine the strain archive (e.g., Paterson et al., 1998, 2016; Žák et al., 2007).

Host rock deformation at various scales similarly records magma transport and intrusion growth processes (e.g., Pollard and Johnson, 1973; Kirkland et al., 2008; Schofield and Totterdell, 2008; Reeves et al., 2018; Magee, 2024; Latimer et al., 2026). The emplacement of magma is inherently linked to deformation of the surrounding crust, induced via localised stress resulting from magma emplacement (e.g., Magee et al., 2019; Memeti et al., 2022; Witcher et al., 2024), or as part of the regional tectonic stress regime (e.g., Jacques and Reavy, 1994; Molina Garza et al., 2021; Koopmans et al., 2025). Fracture analysis in the immediate periphery of an intrusion and its comparison to regional-scale datasets has been shown to be a powerful investigative tool in assessing the control of regional tectonic stress in magma ascent, emplacement and evacuation processes in the apparent absence of tectonic stress (e.g., Kirkland et al., 2008; Latimer et al., 2026). Similarly, the recognition of deformation structures such as forced folds can complement the record of strain preserved within brittle structures in relation to locally induced deformation and the construction of an intrusion (Pollard and Johnson, 1973; Schofield and Totterdell, 2008; Reeves et al., 2018; Magee, 2024). These archives of intrusion emplacement, evolution, and evacuation provide critical insights into the dynamics of magma plumbing systems, eruption behaviour, and the coupling between crustal deformation and magmatism(e.g., Galland et al., 2014; Tibaldi, 2015; Kavanagh, 2018; Burchardt et al., 2022). Yet, multi-scale studies that systematically and quantitatively examine intrusion architecture *and* host rock deformation, and how these relate to regional tectonic structures are relatively uncommon.

The three-dimensional exposure of the Reyðarártindur intrusion, part of a suite of silicic to composite sub-volcanic bodies in SE Iceland (Fig. 1), provides an exceptional natural laboratory to investigate the interplay between magma emplacement, host rock deformation, and evacuation processes (Rhodes et al., 2021, 2024). Here, we integrate rock magnetic techniques (e.g., AMS) and petrology to quantify magmatic and solid-state fabrics within the intrusion and associated subvertical magma-filled fractures in its structural aureole, alongside high-resolution field and UAV-based fracture mapping coupled with mesoscopic fault-slip analysis to characterise brittle deformation in the surrounding lava pile. Together, these datasets allow us to reconstruct magma emplacement and evaluate the role of regional stress in controlling magma transport and eruption pathways. We integrate internal petrofabric data with structural observations from the intrusion's aureole to evaluate magma transport pathways and their relationship to the surrounding fracture network.

Geological setting

The geology of south-eastern Iceland is dominated by Neogene, layered basaltic lavas and associated central volcanic complexes formed during progressive rifting (Fig. 1) (e.g., Torfason, 1979; Saemundsson, 1980). Successions of basaltic lava layers dip gently west to northwest toward the present-day active rift zone, as continued burial by younger flows causes subsidence and rotation of the lava layers toward the rift axis (e.g., Walker, 1974; Saemundsson, 1980; Bodvarsson and Walker, 2007). Burial under elevated geothermal gradients promoted partial melting of the basaltic crust, generating mafic, silicic, and hybrid melts that were transported and emplaced within shallow crustal plumbing systems forming the roots of central volcanoes (Fig. 1) (Sturkell et al., 2003, 2006; Klausen, 2004, 2006; Alfaro et al., 2007; Eriksson et al., 2011; Padilla et al., 2016; Mattsson et al., 2018). These Neogene sub-volcanic plumbing system roots include the silicic Reyðarártindur and Slaufrudalur intrusions, as well as the composite Austurhorn and Vesturhorn complexes (Fig. 1) (e.g., Cargill et al., 1928; Furman et al., 1992; Burchardt et al., 2012; Weidendorfer et al., 2014; Rhodes et al., 2021). This magmatism has been interpreted to relate to propagation of a now-failed rift segment ~6–7 Ma, analogous to the Eyjafjallajökull and Torfajökull central volcanoes in Iceland's present-day neovolcanic zone (Furman et al., 1992).

A regional array of Miocene, NNE-striking normal faults, tensile fractures, and dykes in addition to NW-to-NE-striking strike-slip faults, occur around the central volcanic complexes of southeastern Iceland (Fig. 1) (e.g., Walker, 1974; Torfason, 1979; Saemundsson, 1980; Gudmundsson, 1995; Thorarinsson and Tegner, 2009; Hjartardóttir et al., 2012; Weismüller et al., 2019). Palaeostress reconstructions from these regional structures indicate formation in a Miocene rift-related stress regime, with a sub-horizontal σ_3 oriented broadly ESE–WNW and some rift-parallel shear indicative of a transtensional regime (e.g., Angelier, 1984; Gudmundsson et al., 2002; Clifton and Kattenhorn, 2006; Keiding et al., 2009)(Torfason, 1979; Bergerat et al., 1990; Passerini et al., 1997; Plateaux et al., 2012) (Fig. 1).

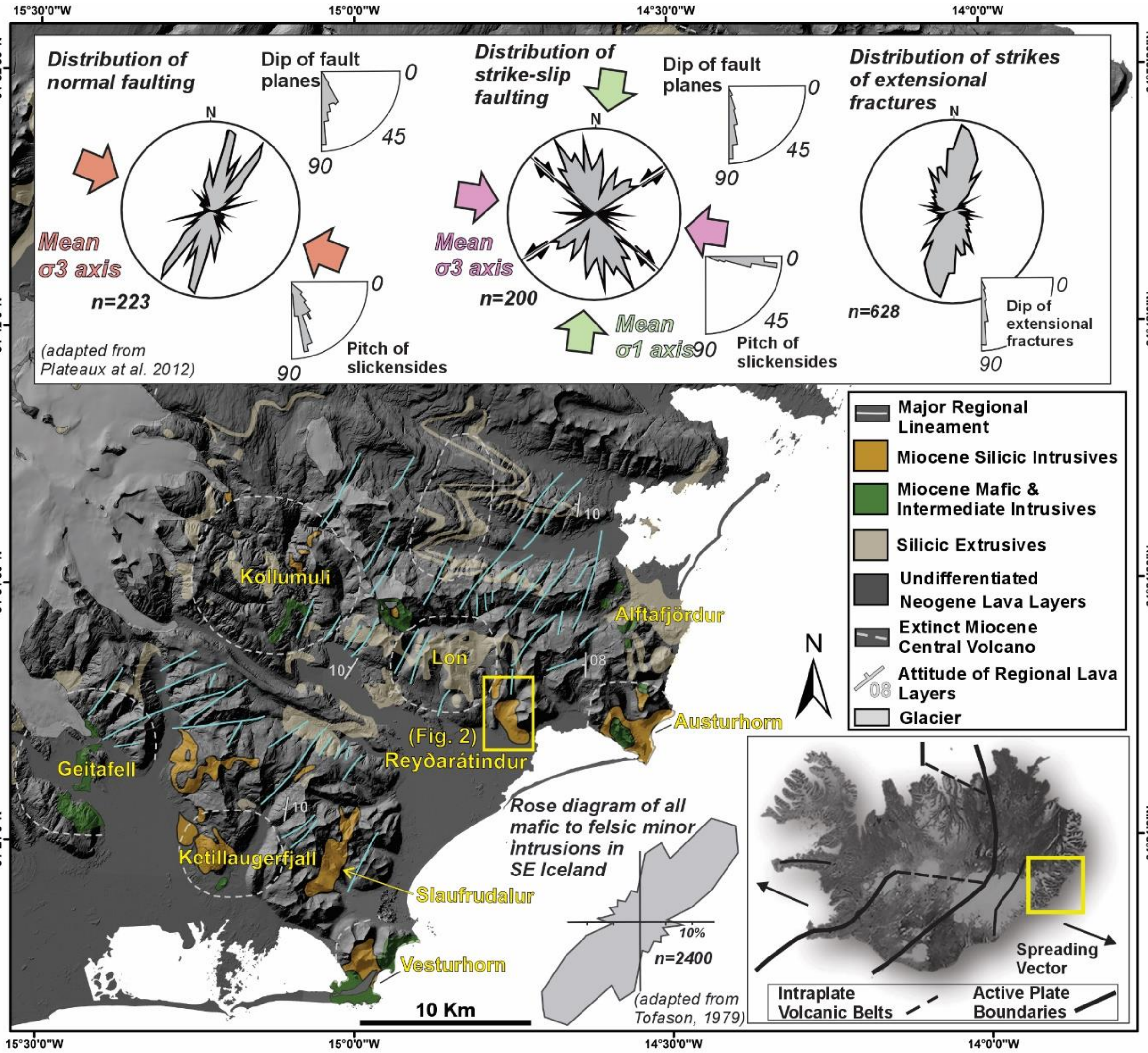

__Fig.1:__ Simplified geological map of exposed Miocene volcanic systems in southeastern Iceland. Inset diagrams compile regional datasets on: normal faults (Top-Left); strike-slip faults (Top-Centre); extensional fractures (Top-Right); and minor intrusions (Bottom-Centre)

(compiled from Walker, 1974; Torfason, 1979; Bergerat et al., 1990; Passerini et al., 1997; Plateaux et al., 2012). Basemap based on data from the National Land Survey of Iceland http://atlas.lmi.is/mapview/?application=DEM.

Exposed by Plio-Pleistocene glacial erosion, the Reyðarártindur intrusion covers an area of approximately 15 km² and reaches a thickness of ~350 m (Fig. 1). Approximately 90–95% of the exposed Reyðarártindur intrusion consists of a macroscopically homogeneous porphyritic granophyric microgranite (Fig. 2) (Rhodes et al., 2021). Most samples display graphic intergrowths of quartz and feldspar radiating around subhedral feldspar and occasional quartz phenocrysts (1–8 mm in size), whilst opaque minerals occur interstitially throughout the groundmass, forming <5 vol.% of the rock (Rhodes et al., 2021). Textural variations and mingling features record multiple magma pulses, particularly evident in scoured river channels at the lowermost exposures, where a mafic-silicic composite zone, similar to the 'Net Veined Complex' of the neighbouring Austurhorn Complex is exposed (Fig. 2) (e.g., Furman et al., 1992; Weidendorfer et al., 2014; Rhodes et al., 2021). The uppermost exposed roof contact of Reyðarártindur intrusion is flat-lying to gently dipping (~00–15º NNE), parallel to the overlying basaltic lava layers. Whilst the basaltic lava layers of the surrounding host rock regionally dip gently to the west at approximately ~5–15° (e.g., Walker, 1960), lava dips are locally >30° (Rhodes et al., 2024). The Reyðarártindur intrusion has been interpreted to have steep lateral boundaries, which are occasionally stepped (Rhodes et al., 2021; Rhodes et al., 2024). The roof rock locally contains (conjugate) sets of fractures and faults that broadly strike either NE-SW, NW-SE, or E-W; some faults and fractures are intruded by granitic dykes (Rhodes et al., 2024).

Overall, the Reyðarártindur intrusion is interpreted as a shallow-level pluton, emplaced within a broader volcanic plumbing system in south-eastern Iceland (Walker, 1960; Blake, 1966; Rhodes et al., 2021). Geochronological analyses from five sampling localities across the western exposure of the Reyðarártindur intrusion yield a weighted mean SHRIMP $^{206}Pb/^{238}U$ zircon age of 7.30 ± 0.06 Ma (Padilla, 2015), closely comparable to three U-Pb zircon ID-TIMS ages of 7.44 ± 0.019 Ma, 7.448 ± 0.009 Ma and 7.424 ± 0.033 Ma obtained from the roof, middle and lower structural levels of the intrusion, respectively (Twomey, 2023). Based on observed magma mingling textures, with limited evidence of hybridization, and lack of significant chilled margins, Rhodes et al., (2021) developed simple thermal models that suggest the intrusion may have intruded and erupted within ~1,000 years. Rhodes et al. (2024) proposed the Reyðarártindur intrusion developed a magmatic overpressure during emplacement that caused minor uplift, significant aseismic subsidence, and roof fracturing that ultimately triggered roof collapse and surface graben formation.

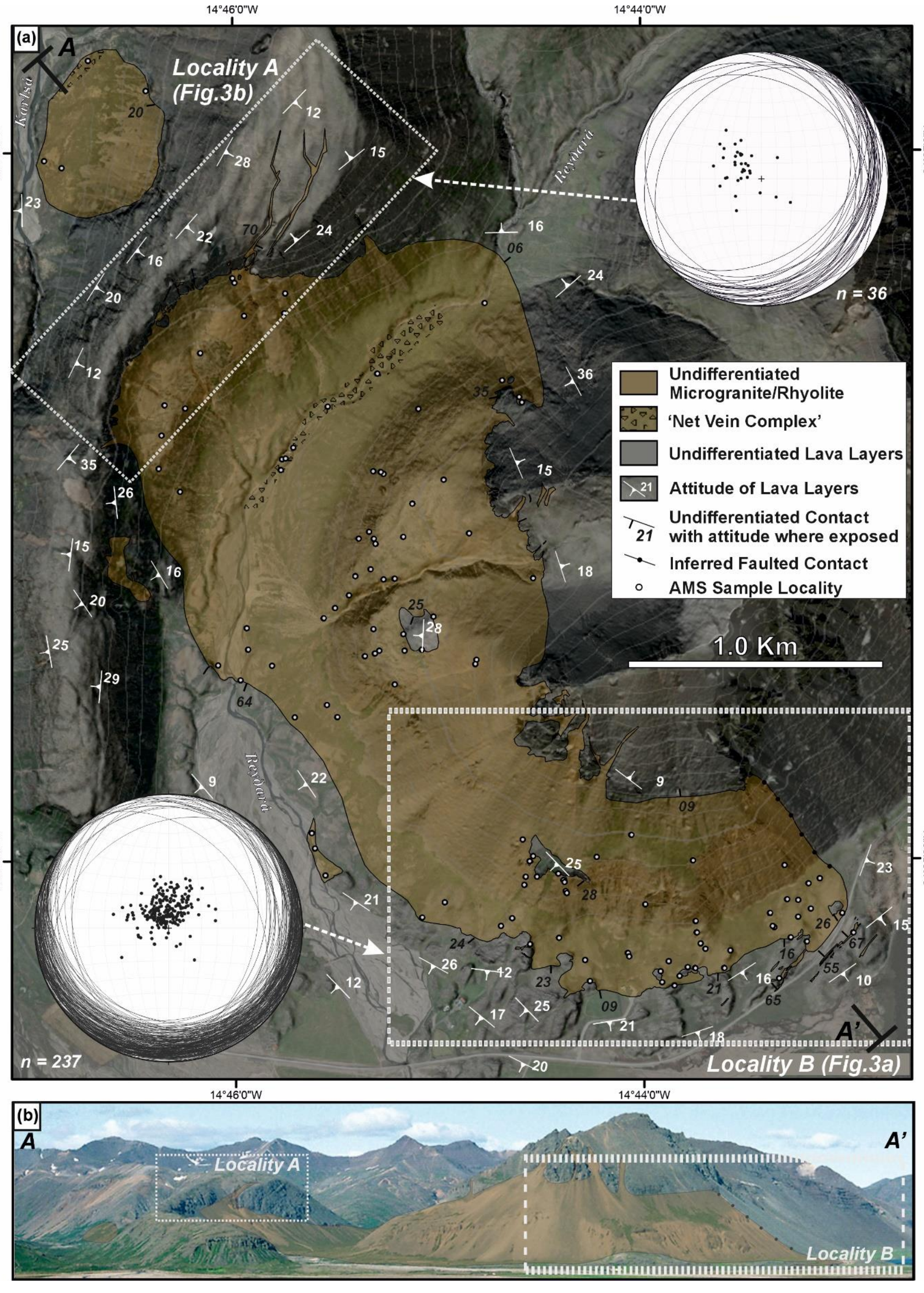
14°46'0"W
14°44'0"W
64°27'0"N
64°25'30"N
(a)
A
A'
Locality A
(Fig.3b)
Locality B (Fig.3a)
Kaviksá
Reyðará
n = 36
n = 237
1.0 Km
Undifferentiated
Microgranite/Rhyolite
'Net Vein Complex'
Undifferentiated Lava Layers
Attitude of Lava Layers
Undifferentiated Contact
with attitude where exposed
Inferred Faulted Contact
AMS Sample Locality
(b)
Locality A
Locality B

Fig.2: (a) Geological map of the Reyðarártindur intrusion. Inset stereographic projections display the attitude of the layered basalts in the surrounding structural aureole in two selected localities (Localities A and B). (b) View towards NE showing cross-sectional exposure of the intrusion, with Localities A and B highlighted in dashed boxes.

Methods

Field mapping and sampling

Lithological and structural mapping of the intrusion and surrounding host rock was conducted with an iPad tablet using the FieldMOVE^{TM} application (https://www.mve.com/digital-mapping/). Lithological mapping was focused on petrographic variation across the Reyðarártindur intrusion, with structural mapping constraining features related to the structural aureole of the intrusion adjacent to the host rock contact. Structural data such as fault, fracture, contact and host rock orientation were measured with the digital compass clinometer within FieldMOVE^{TM} and regularly validated with an analogue compass adjusted for the magnetic declination in the area. These data were supplemented with unmanned aerial vehicle photogrammetry fracture analysis, described below. All data was processed in ArcMap to create a detailed geological map of the Reyðarártindur intrusion (e.g., Fig. 2).

Field mapping and fracture analysis results were used to guide a targeted block sampling campaign for anisotropy of magnetic susceptibility and complementary petrographic thin section analysis. Samples were collected along an even grid across the pluton (outcrop permitting) and along a selection of peripheral sheet intrusions that are thought to represent magma venting conduits (Fig. 2).

Unmanned aerial vehicle (UAV) photogrammetry

Unmanned aerial vehicle (UAV) photogrammetry was adopted as a complementary method to field-based structural mapping, particularly where cliff exposure or access restrictions limited direct measurement. The approach follows established Structure-from-Motion (SfM) workflows for geological and structural mapping, in which overlapping georeferenced aerial images are processed to generate high-resolution orthomosaics, dense point clouds and digital elevation models suitable for extracting fracture and fault geometries (e.g., Bemis et al., 2014; Vollgger and Cruden, 2016; Bonali et al., 2019; Bonali et al., 2020). UAV surveys focused on the intrusion margins and adjacent structural aureole, with particular emphasis on areas with steep fracture networks and magma-filled sheets exposed.

Aerial imagery was acquired using a DJI Phantom III Professional quadcopter equipped with a 12.4 megapixel digital camera mounted on a three-axis gimbal. This device was selected because it allowed low-altitude, stable image acquisition above irregular terrain and sufficient manoeuvrability to follow the geometry of intrusion contacts and host rock discontinuities. Flights were planned to maintain near-nadir camera orientations over map-view exposures and to maximise image overlap across steep or irregular outcrops. Flight altitudes ranged between 40 to 60 m above ground level, compromising between spatial resolution, areal coverage and battery endurance, while accommodating for local topography and wind conditions. Image acquisition was conducted along parallel flight lines with approximately 70% forward and lateral overlap, producing continuous image coverage.

Raw UAV imagery was processed in Pix4Dmapper Pro using a standard SfM workflow comprising image alignment, sparse point-cloud generation, camera calibration optimisation, dense point-cloud construction, digital elevation model generation, and orthomosaic production. The resulting photogrammetric outputs were then exported for structural interpretation and mapping, with georeferencing based on embedded image-position metadata from the UAV GPS and checked against field observations and the spatial continuity of structures between overlapping image blocks. In the absence of an independent ground control point network, the UAV-derived products provide internally consistent mapping and measurement surfaces suitable for relative structural analysis. The reliability of UAV fracture trace data and mapped structures was verified through comparison with outcrops and fractures mapped in the field with compass clinometer and FIELDMOVE.

Photogrammetric datasets were imported into SiroVision 6.2 and ArcMap for structural mapping and quantitative analysis. The othromosaics were used to trace planar discontinuities, including faults, joints, lithological contacts, sheet margins, and basaltic lava-layer surfaces in plan-view. As many structures were mapped from orthophotographs, and displacement cannot be confidently determined everywhere, we refer to image-derived traces as lineaments unless field observations demonstrate fault slip, opening, or a magmatic sheet margin. Lineaments were manually digitised only where traces were sharp, continuous and clearly expressed, or where their interpretation could be supported by field observations. Lineaments were classified according to orientation, trace length, continuity, cross-cutting relationships, association with magma-filled sheets, and evidence for displacement or opening. Where lineaments, sheet margins or lava-layer surfaces were sufficiently exposed on 3D surface models, structural measurements were extracted as dip/dip direction and strike in SiroVision 6.2. UAV-derived measurements were compared with analogue compass and FieldMOVE measurements collected at accessible outcrops to evaluate measurement reliability and to avoid duplicating the same structure across overlapping image blocks. The final lineament dataset was compiled with field measurements in ArcMap to produce geological and structural maps, rose diagrams and lower-hemisphere stereographic projections, enabling comparison between UAV-derived structures, anisotropy of magnetic susceptibility (AMS) fabrics and the wider regional structural framework.

Anisotropy of magnetic susceptibility (AMS)

Anisotropy of magnetic susceptibility (AMS) allows the rapid and precise measurement of magnetic fabrics (D. H. Tarling and Hrouda, 1993). AMS fabrics are recognised as useful petrofabric data sets with applications in magma transport (Knight and Walker, 1988; Archanjo et al., 1994; Stevenson et al., 2007b), magmatic mineral layering (O'Driscoll et al., 2024; Jones et al., 2025), tectonic deformation (Petronis et al., 2012; McCarthy et al., 2015; Burton-Johnson et al., 2019; Knight et al., 2024). For example, increasing velocity gradients adjacent to sheet margins can lead to the development of crystal fabrics through processes such as rotation and imbrication during magma flow; these fabrics can be measured using AMS and related to magma flow direction; i.e. the intersection point of imbricated fabrics is considered to be orthogonal to the flow direction (e.g., Knight and Walker, 1988; Callot et al., 2001; Geoffroy et al., 2002; Köpping et al., 2023).

AMS analyses involve measuring of the bulk magnetic susceptibility of an individual sample along multiple axes to determine a 3D susceptibility tensor defined by three orthogonal principal axes ($K_1 \geq K_2 \geq K_3$) (D. H. Tarling and Hrouda, 1993). The maximum axis (K_1) defines the magnetic lineation, this is usually parallel to the crystallographic or grain shape long axis depending on the dominant mineral carrier of AMS (D. H. Tarling and Hrouda, 1993). The short axis (K_3) commonly defines the pole to the magnetic foliation plane (i.e., the K_1-K_2 plane). The mean susceptibility (K_m), shape (T_j), and strength (or ellipticity; P_j) of the ellipsoid is quantified using the following parameters:

$$Km = (K_1 + K_2 + K_3)/3$$

$$P_j = \exp\sqrt{2[(\eta_1 - \eta_m)^2 + (\eta_2 - \eta_m)^2 + (\eta_3 - \eta_m)^2]}$$

$$T_j = \frac{2\eta_2 - \eta_1 - \eta_3}{\eta_1 - \eta_3}$$

where

$\eta_x = \ln(k_x)$, x = 1, 2, 3, and $\eta_m = \frac{(\eta_1 + \eta_2 + \eta_3)}{3}$

The shape of the ellipsoid ranges from perfectly oblate ($T_j = +1$) to perfectly prolate ($T_j = -1$) (Jelinek, 1981).

The mineral that dominates bulk magnetic susceptibility does not necessarily control AMS; a lower-susceptibility mineral can dominate the anisotropy if magnetite crystals have an isotropic distribution and orientation (Biedermann and Bilardello, 2021). Deviatoric susceptibility (***K'***) was calculated to assess which mineral phase is the dominant carrier of AMS (Jelinek, 1984, Jelinek, 1984; Biedermann et al., 2014; Koopmans et al., 2022; Latimer et al. 2024):

$$\boldsymbol{K'} = \sqrt{\left\{\frac{\left(K_1 - K_{\{mean\}}\right)^2 + \left(K_2 - K_{\{mean\}}\right)^2 + \left(K_3 - K_{\{mean\}}\right)^2}{3}\right\}}$$

Where ***K'*** represents the deviation of the AMS ellipsoid from a sphere with a diameter defined by mean susceptibility (Kmean), thus removing the contribution of isotropic materials from anisotropy measurements.

In this study, AMS data were collected from a total of 127 sample sites, both within the intrusion (119 sample sites) and three adjacent inclined sheets (8 sample sites) to determine magma flow patterns and investigate the relationship in emplacement dynamics between the intrusion and adjacent inclined sheets (Fig. 2). Although the sampling localities across the intrusion were partly determined by outcrop accessibility, samples were collected across the length and height of the main body of the intrusion wherever possible.

Oriented block samples were collected at each sample site from which 7 to 22 (average 12) 22 mm by 25 mm right cylinder core sub-specimens were extracted using a rock coring drill press and a diamond-tipped, nonmagnetic saw blade. The sub-specimen data was averaged for each block following the procedure of Jelinek (1978) to produce mean values of the AMS ellipsoid. The three principal axis directions for each block sample are plotted stereographically within 95% confidence limits. All AMS measurements were carried out using an automated 3D rotator attached to a KLY-5a Kappabridge operating at a low alternating field of 400A/m at 1220 HZ at the University of St. Andrews M^3Ore Laboratory. The localities of the sheets sampled are marked in Localities A and B within Figure 2.

Rock magnetic experiments

The interpretation of AMS data is subject to several caveats. For instance, if the AMS were dominated by elongated single-domain magnetite grains, an inverse AMS fabric could develop, in which the maximum susceptibility axis (K1) is oriented perpendicular to the particle elongation direction (Potter and Stephenson, 1988; Rochette et al., 1992, 1999). If left undetected, the presence of inverse fabrics may compromise interpretation of the AMS fabric and the arising magma flow model (D. H. Tarling and Hrouda, 1993; Borradaile and Jackson, 2010). To aid the interpretation of AMS data, all AMS results were compared to observed mineral fabrics and thermomagnetic experiments were conducted on 15 representative samples from across the intrusion to inform on the composition of mineral phase(s) that control magnetic susceptibility (Hrouda et al., 1997). Hysteresis and isothermal remanent magnetisation data were also collected on 6 representative samples to assess the coercivity spectra of our samples to determine if minerals likely to carry an inverse mineral fabric were present (Day et al., 1977; Dunlop, 2002).

Thermomagnetic experiments require each sample to be powdered in a ceramic pestle and mortar, a 0.3 g powder subsample underwent a three-step heating/cooling regime as follows: 1) heating from -196°C to 0°C using a CS-L cryostat KLY5-a attachment; 2) heating 25°C to 700°C and cooling back to 40°C using CS4 furnace attachment. An argon atmosphere was maintained to minimise sample oxidisation during step 2. Curie point and Verwey transitions were estimated from the heating-cooling curves using either the Hopkinson Peak (Hopkinson, 1890) or inflection point methods (Tauxe, 1998) these transitions can be used to interpret the magnetic mineralogy of each sample and determine which mineral phases contribute to magnetic susceptibility (D. Tarling and Hrouda, 1993). (Dunlop and Özdemir, 1997)

Magnetic hysteresis loops were measured to test for the presence of single domain grains which could result in inverse magnetic fabrics. Samples were first demagnetized in a 1960 mT field and subsequently subjected to bidirectional magnetic fields up to 300–1000 mT. Hysteresis data were processed in HystLab (Paterson et al., 2018), including correction for instrumental drift and removal of the paramagnetic high-field slope using the linear high-field fitting procedure. Saturation magnetisation (Ms), saturation remanent magnetisation (Mrs), and coercive force (Bc) were determined from the arising data (Dunlop & Özdemir, 1997; Paterson et al., 2018). Isothermal Remanent Magnetisation (IRM) data was measured to calculate the saturation IRM (sIRM) and coercivity of remanence (Bcr) of samples (Dunlop & Özdemir, 1997). Samples were first demagnetized in a 1960 mT field and subsequently subjected to a unidirectional magnetic field up to 1000 mT to measure sIRM. Once 1000 mT was reached, the samples were then magnetised in the opposite direction, again to 1000 mT with Bcr defined as the field required to fully demagnetise the sample (Dunlop & Özdemir, 1997; McCarthy et al., 2015).

Results

Intrusion geometry & host rock structure

An approximately 370 m thick section of the Reyðarártindur intrusion is exposed from its roof contact downward, but its base is not observed, leaving both its true thickness and the nature of contact between the intrusion floor and surrounding host unknown (Fig. 2). Our mapping confirms basaltic lavas within in the structural aureole of the Reyðarártindur intrusion generally dip gently to moderately (~09–29°) outwards, away from the exposed centre of the intrusion (Figs. 2 – 4). However, at the SE contact, the host rock basalts are deflected into parallelism with the SSE intrusion contact margins and dip between ~05–60° to define a ~1 km wide gently up-domed monoclinal structural aureole (Locality B; Figs. 2 and 3a), akin to an intrusion-induced, gently domed ‘forced fold’ structure. Two basalt lava outcrops situated on the western flank of the intrusion dip moderately to the WSW forming part of the domed wall rock structure (Figs. 2 and 3a). Although the intrusion contact is broadly parallel to layered lava dips at map-scale, locally (tens of metres) the intrusion contact is observed to cut the lava layers along steeply inclined NNE-SSW fracture planes, consistent with previous reports (Fig. 3b). In the east of the intrusion the host rock contact is steeply inclined and truncates the gently inclined basaltic lavas, which we interpret to be a faulted contact, in line with that of Rhodes et al. (2021) (Fig. 2). The basalt layers around the NW of the laccolith also deviate from the majority of the host rock contact in that they dip to the ESE, towards the interior of the intrusion, these may represent collapsed blocks of host rock (Fig. 3b) (Rhodes et al., 2021, 2024).

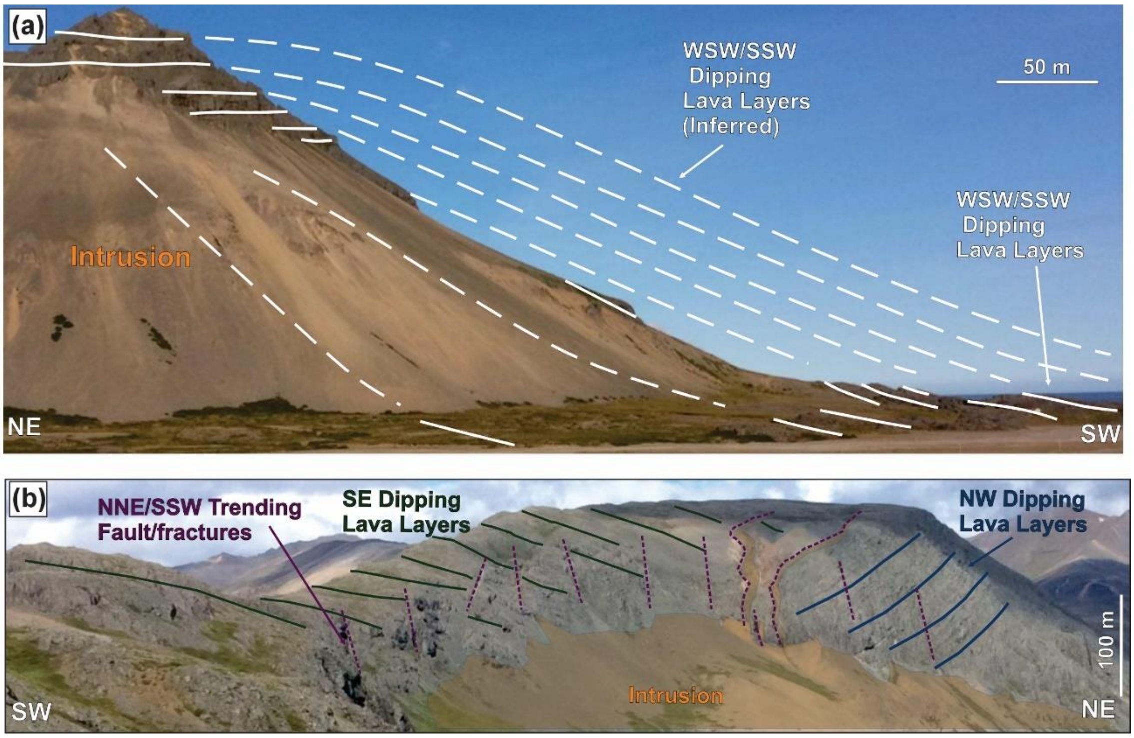

Fig. 3: *(a) View looking towards the ESE showing the domed forced fold geometry of the SSE structural aureole. (b) View looking towards the WNW showing the gentle dip of layered basalts above the intrusion that dip inward towards the interior. WNW trending inclined sheets emanating from the main body of the intrusion are also evident.*

Lineaments and sheet intrusions

Field mapping and UAV data reveal a prominent network of lineaments within and around the structural aureole of the Reyðarártindur intrusion (Twomey et al., 2026) (Fig. 4); these lineaments correspond to fractures, faults, and sheet intrusions. A total of 321 lineaments were measured, defining three principal sets: NE-SW (~040–070°), NNW-SSE (~350–020°), and sub-ordinate WNW-ESE (Fig. 4). The dip values of lineaments in all sets range from gently to steeply inclined and, collectively, define a left-stepping sigmoidal pattern at outcrop scale, particularly near the southern pluton contact (Fig. 4). Field observations demonstrate that steeply inclined silicic sheets, tens to hundreds of meters long and <1–12 m thick, locally occur along the trace of some fractures or faults (Figs. 2, 3b, 4). These sheets extend outward from the main intrusion and predominantly trend NE-SW, parallel to one of the mapped lineament sets (Fig. 4). Two areas display particularly well-developed magma-filled fractures: the first along the NW margin (Locality A; Figs. 2-4), and the second in the SW sector (Locality B; Figs. 2-4).

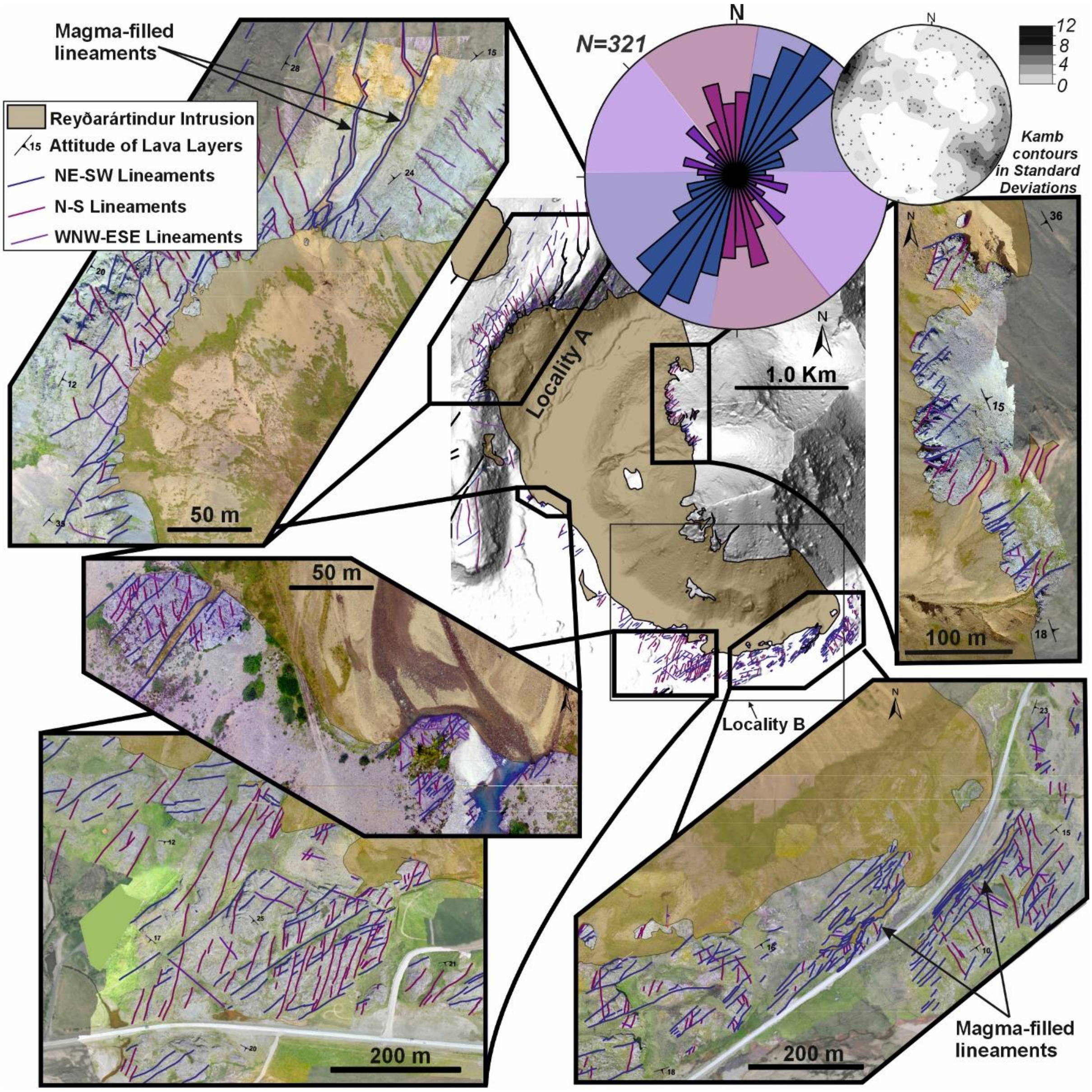

Fig.4: *High-resolution orthophotographs showing the exposed contact of the Reyðarártindur intrusion with the surrounding lava layers and associated lineaments. map of lineaments. Orientation sets are colour-coded and plotted on a rose plot (bin size 5º) with a corresponding stereographic projection of their attitudes.*

Petrographic observations

The Reyðarártindur intrusion is petrographically dominated by a relatively restricted set of silicic facies, with variations primarily reflecting textural state, crystal content, and degrees of magma mingling rather than fundamentally different lithologies, as described in detail by Rhodes et al. (2021).

The dominant facies is a granophyric granite to microgranite, which forms the bulk of the intrusion (Figs. 2, 5a-d). This facies is fine-grained and commonly exhibits pervasive micrographic (granophyric) intergrowths of quartz and alkali feldspar, with 4-8 mm plagioclase phenocrysts, minor biotite and amphibole, and accessory Fe–Ti oxides and zircon (Fig. 5f & h). A banded rhyolite occurs in structurally higher parts of the intrusion and within inclined sheets. It is characterised by 1–5 mm compositional and textural banding defined by aligned quartz and feldspar crystals (Fig 5e-f). The net-veined complex is a composite hybrid zone in the lowest exposed structural levels of the intrusion, characterised by angular to ovoid enclaves of intermediate composition set within a granophyric microgranite matrix of intermediate to silicic. Contacts between included enclaves are often cuspate, and may be rimmed or penetrated by granophyric material (Fig. 5g).

Across all facies, Fe-Ti oxides occur as minor (~0.5–5 vol%) interstitial crystals or as inclusions within plagioclase and hornblende phenocrysts (Fig. 5). The long axes of Fe–Ti oxide grains are observed parallel to the long axes of their host plagioclase and amphibole crystals (Fig. 5). Fe-Ti oxides within the 'Net-veined complex' are also locally intergrown or included within elongate tabular hornblende crystals (Fig. 5d, f, h). Abundant graphic intergrowths of quartz and feldspar around phenocrysts of feldspar and hornblende with included Fe-Ti oxides preserved across the intrusion suggest rapid crystallisation under undercooled conditions and the preservation of magmatic fabrics and textures. (Rhodes et al. 2021).

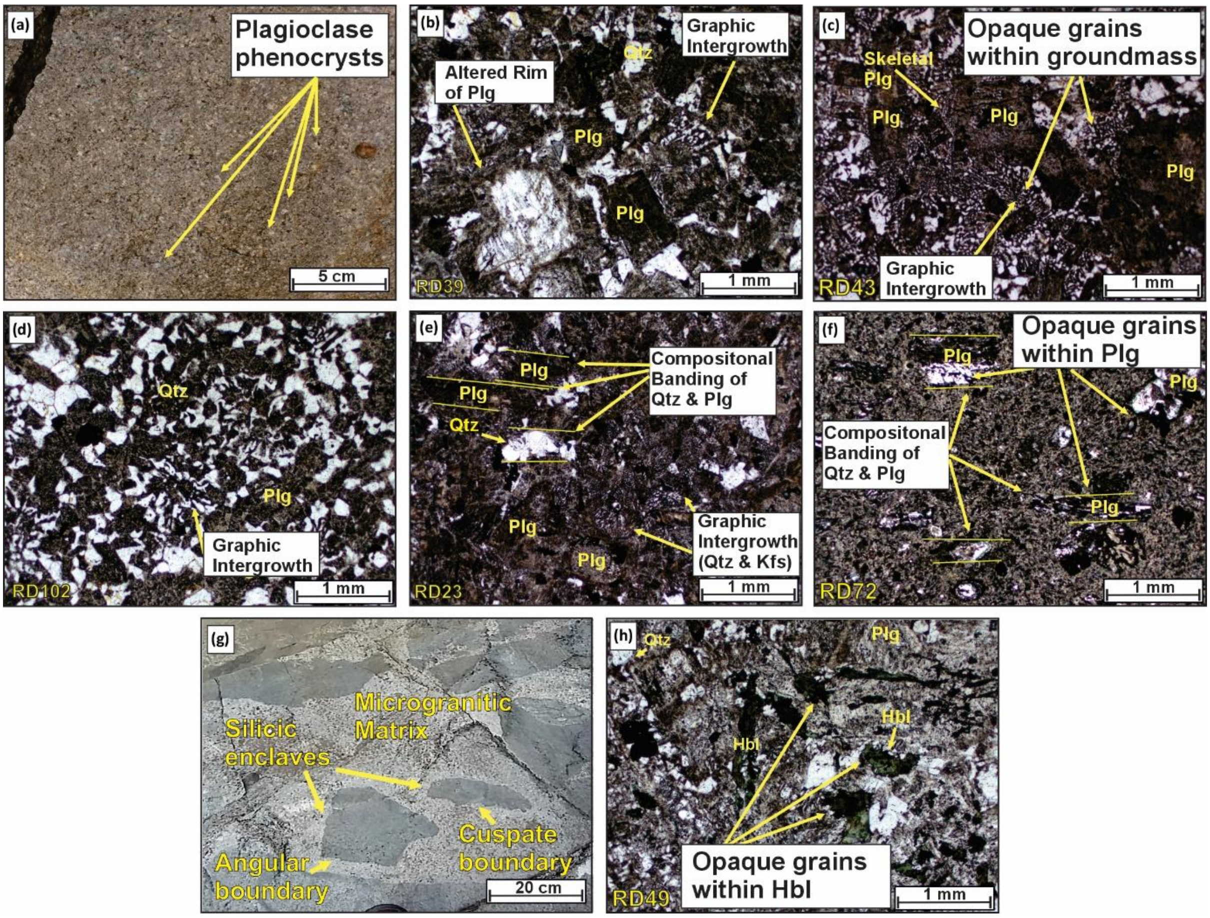

Fig.5: *(a) representative outcrop photo of Microgranite. (b-f) Representative cross-polarized light (XPL) microphotographs demonstrating the characteristic petrographic features of the granophyric, fine-grained granite/microgranite and textural rhyolite. distributed across the intrusion. Black minerals represent opaques in thin section. (g) Representative photo of 'Net-Veined complex'. (h) Microphotograph of a hornblende trachydacite from an enclave within the 'Net-Veined complex'.*

Rock magnetic results

A summary of rock magnetic analysis results is provided here, and a full data table is available in the Supplementary Material (Twomey et al., 2026).

Characterisation of dominant magnetic mineralogy

Continuous susceptibility versus temperature dependency experiments consistently show two abrupt features on the heating-cooling curves (Fig.6a): (i) an abrupt increase in susceptibility between -175°C to -150°C before the susceptibility curve plateaus up to the ambient room temperature, marking Verwey Phase transition for magnetite (Verwey and Haayman, 1941); and (ii) a later abrupt decrease in susceptibility between 575-580°C corresponding with the Curie temperatures (Tc) for a very low Ti titanomagnetite (0.1% < Ti content < 1.0%) or near-stoichiometric magnetite (Ti < 0.1%) as the dominant magnetic minerals (Akimoto, 1962; Tauxe, 1998; Lattard et al., 2006; Getzlaff, 2008). Several samples display a peak in susceptibility at ~470–480°C with a subsequent secondary peak at 575-580°C during heating (Fig. 6a), consistent with a low titanium titanomaghemite phase where exsolution of Ti between 500–700°C resulted in modification of the 470–480°C peak on the cooling curve and a more prominent ~580°C magnetite curie point (Akimoto, 1962; Dunlop and Özdemir, 1997). A minority of samples show a <10% increase in bulk susceptibility between 270°C and 340°C during heating, this feature is always absent on the cooling curve and a 5–20% increase in bulk susceptibility is observed after cooling (Fig. 6a). The increase in susceptibility is associated with the growth of new magnetite during the experiment and we thus attribute the 270°C and 340°C heating curve inflection to the breakdown of an iron sulphide minerals such as pyrite (Dunlop and Özdemir, 1997).

Results of coercivity spectra analysis are summarised in Fig. 6. Initial sIRM curves show an exponential increase in remanent magnetisation (Mr) between 0 – 100 mT with almost all samples reaching 90% saturation between 200 – 250 mT, compatible with the presence of pseudosingle domain to multidomain magnetite. Sample VT18RD002 is the exception where a field of ~500 mT is required before 90% saturation is achieved. Most samples show a modest increase in magnetisation between 250 mT and 800 mT, indicative of a minor contribution to remanence by a hight coercivity mineral such as maghemite. A Day plot of hysteresis results illustrates that all samples plot in the pseudosingle domain to multidomain fields (Fig. 6) (Day et al. 1977).

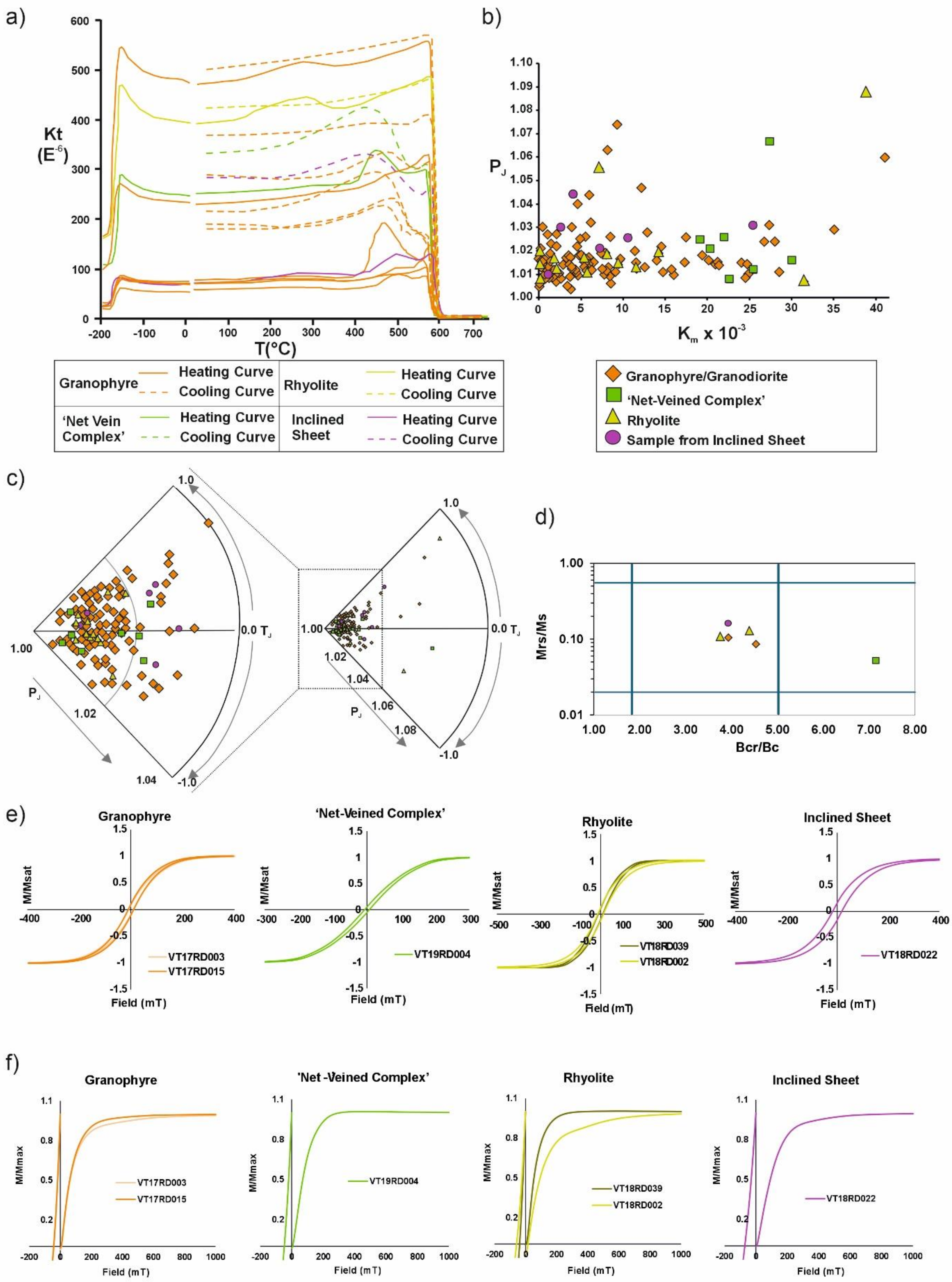

a)
Kt (E-6)
T(°C)
Granophyre Heating Curve Cooling Curve
Rhyolite Heating Curve Cooling Curve
'Net Vein Complex' Heating Curve Cooling Curve
Inclined Sheet Heating Curve Cooling Curve
b)
PJ
Km x 10-3
Granophyre/Granodiorite
'Net-Veined Complex'
Rhyolite
Sample from Inclined Sheet
c)
PJ
0.0 TJ
1.0
-1.0
d)
Mrs/Ms
Bcr/Bc
e)
Granophyre
'Net-Veined Complex'
Rhyolite
Inclined Sheet
M/Msat
Field (mT)
VT17RD003
VT17RD015
VT19RD004
VT18RD039
VT18RD002
VT18RD022
f)
Granophyre
'Net -Veined Complex'
Rhyolite
Inclined Sheet
M/Mmax
Field (mT)
VT17RD003
VT17RD015
VT19RD004
VT18RD039
VT18RD002
VT18RD022

Fig. 6: *(a) Results of temperature dependent low-field magnetic susceptibility experiments. (b)Plot of Pj vs Km. (c) Polar plot of Tj vs Pj data. (d) Modified Day plot of coercivity spectra data. (e) Plot of hysteresis loop data. (f) Plot of Isothermal Remanent Magnetisation data.*

Anisotropy of Magnetic Susceptibility (AMS) results

The average bulk susceptibility (K_{m}) (Jelinek, 1981)of the 127 samples measured is 9.24 x 10^{-3} SI, ranging from 7.92 x 10^{-5} SI to 4.12 x 10^{-2} SI (Fig. 6b). The 'net-veined' complex in the lowermost exposed section of the intrusion generally has higher K_m values (191 – 412 x 10^{-3} SI) (Fig. 6c). The corrected degree of anisotropy (P_j) (Jelinek, 1981) varies between 1.004 and 1.088, averaging at 1.018 with no overall distinguishing pattern across the intrusion. Shape factor (T_j) (Jelinek, 1981) values vary between -0.94 and 0.91 with a 0.09 average; 52 samples are predominately prolate ($T_j<1$) and 72 are dominantly oblate ($T_j>1$). Both P_j and T_j values show no defined pattern with respect to K_m (Fig. 6b – c). This shows that the shape and orientation of the AMS fabric is independent of bulk susceptibility and the relative abundance of magnetite in this set of samples.

Deviatoric susceptibility (K′) varies from 2.91 × 10^{-7} to 1.33 × 10^{-3}, i.e., several orders of magnitude greater than single-crystal values of hornblende (1.19 ×10^{-8}), biotite (4.96 × 10^{-8}) and feldspar (1.60 × 10^{-9}) (Table S3; Biedermann et al., 2014, 2015, 2016). Together with the magnetic characterization data and petrographic observations, this result shows that AMS in all sites are dominated by pseudosingle domain to multidomain magnetite.

AMS fabric distribution

A stereographic projection of all AMS fabric data reveal that K_1 trends throughout the entire intrusion predominantly plot along an NNE–SSW axis and are mainly clustered into gently (~0–36º) and steeply (~55–90º) inclined populations (Fig. 7). The gently plunging, NE-SW trending K_1 axes typically occur: (i) along the south-eastern lowermost exposure of the intrusion (Locality B); (ii) within a NW-SE trending linear zone located towards the centre of the intrusion exposure; and (iii) near the base of inclined sheets that extend up from the north-western margin of the main intrusion (Locality A) (Fig. 7). Interspersed with these NE-SW trending, gently plunging K_1 axes are steeply inclined magnetic lineations with variable plunge directions (Fig. 7). For example, in Locality A, a concentration of steep NW-SE trending K_1 axes are aligned adjacent to the NW contact (Fig. 7).

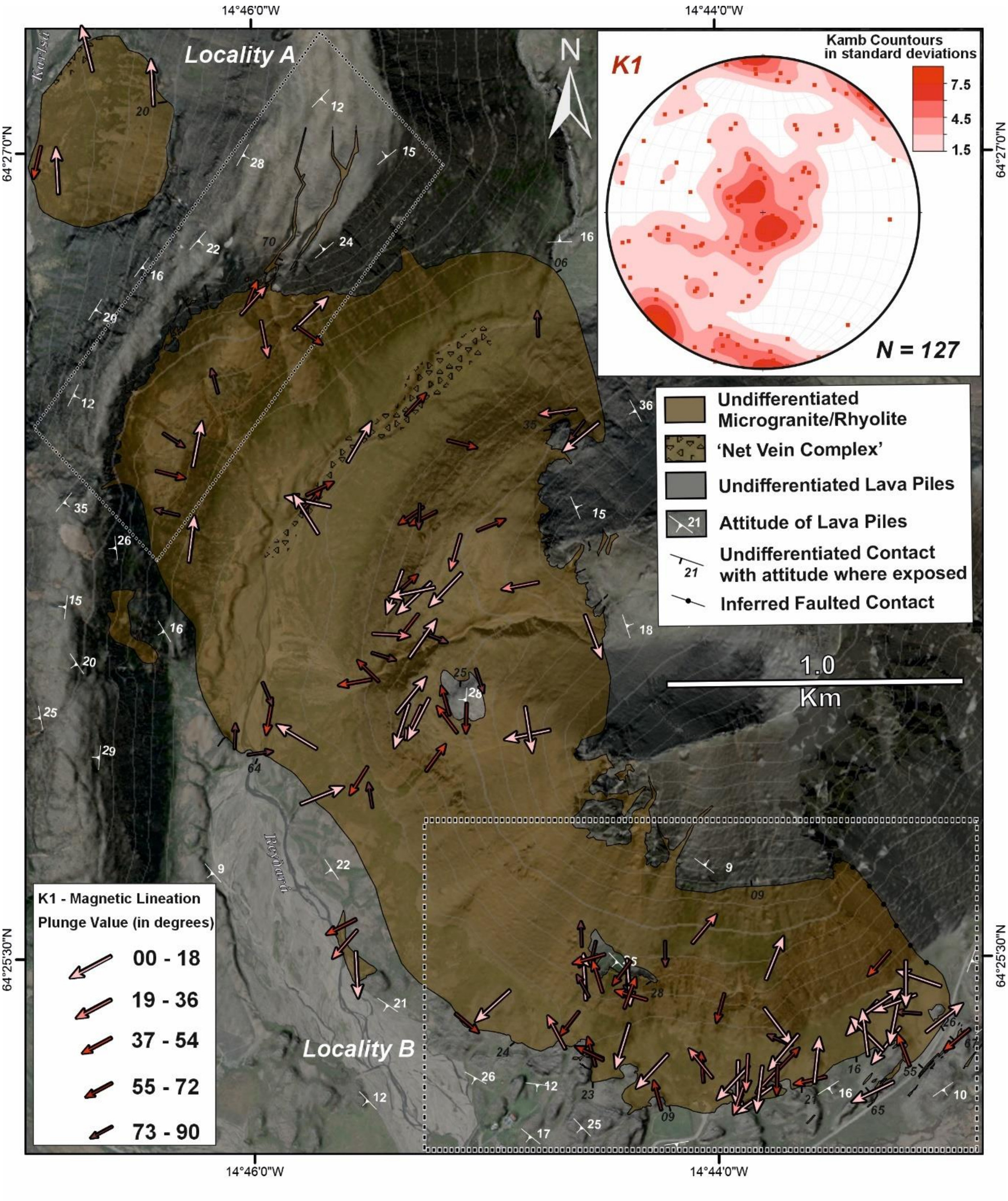

Fig. *7: Map of the Reyðarártindur intrusion plotting K1 magnetic lineations. The degree of inclination of the K1 plunge is colour coded.*

A stereographic projection of K_3 axes (i.e., pole to K_1-K_2 plane) from across the intrusion also show two distinct clusters of foliations, one that is gently inclined (vertical K3) and one that is subvertical, striking NNW/ SSE (Fig. 8). Gentle to moderate dips of magnetic foliations typically occur along the lower intrusion margin and at an outlier to the northwest of the intrusion (Fig. 8). Several examples of magnetic fabrics appear to not correlate with the dominant NNE–SSW fabrics prevalent across the intrusion (Figs. 7 and 8). For instance, magnetic foliations immediately bordering the exposed SSE edge or close to the roof in the centre of the intrusion often strike sub-parallel/parallel to the orientation of the adjacent contact (Fig. 8). Furthermore, magnetic lineations (K_1) in the structurally lower north-northwest exposures (including both the 'net-veined' complex and the northwest outlier) occasionally trend shallowly towards the NNW, parallel to the magnetic foliation (Figs. 7 and 8). In other parts of the northwest exposure, particularly the structurally higher sections, lineations are generally steep to sub-vertical with the equivalent foliations striking very steeply towards the NE–SW (Fig. 8). Towards the centre and to the NW of the intrusion exposure, a concentration of lineations trend gently to moderately towards the SW, with foliations orientated NNE–SSW, corresponding with the dominant NNE–SSW magnetic fabric axis (Figs. 7 and 8). Towards the southeast exposure, lineations locally plunge gently towards the SSE, sub-parallel to the NNW-SSE strike of the corresponding foliation (Figs. 7 and 8). Overall, in plan-view the plunge axis and strike of the magnetic lineations and foliations, respectively, appear to diverge towards the SW (Figs. 7 and 8).

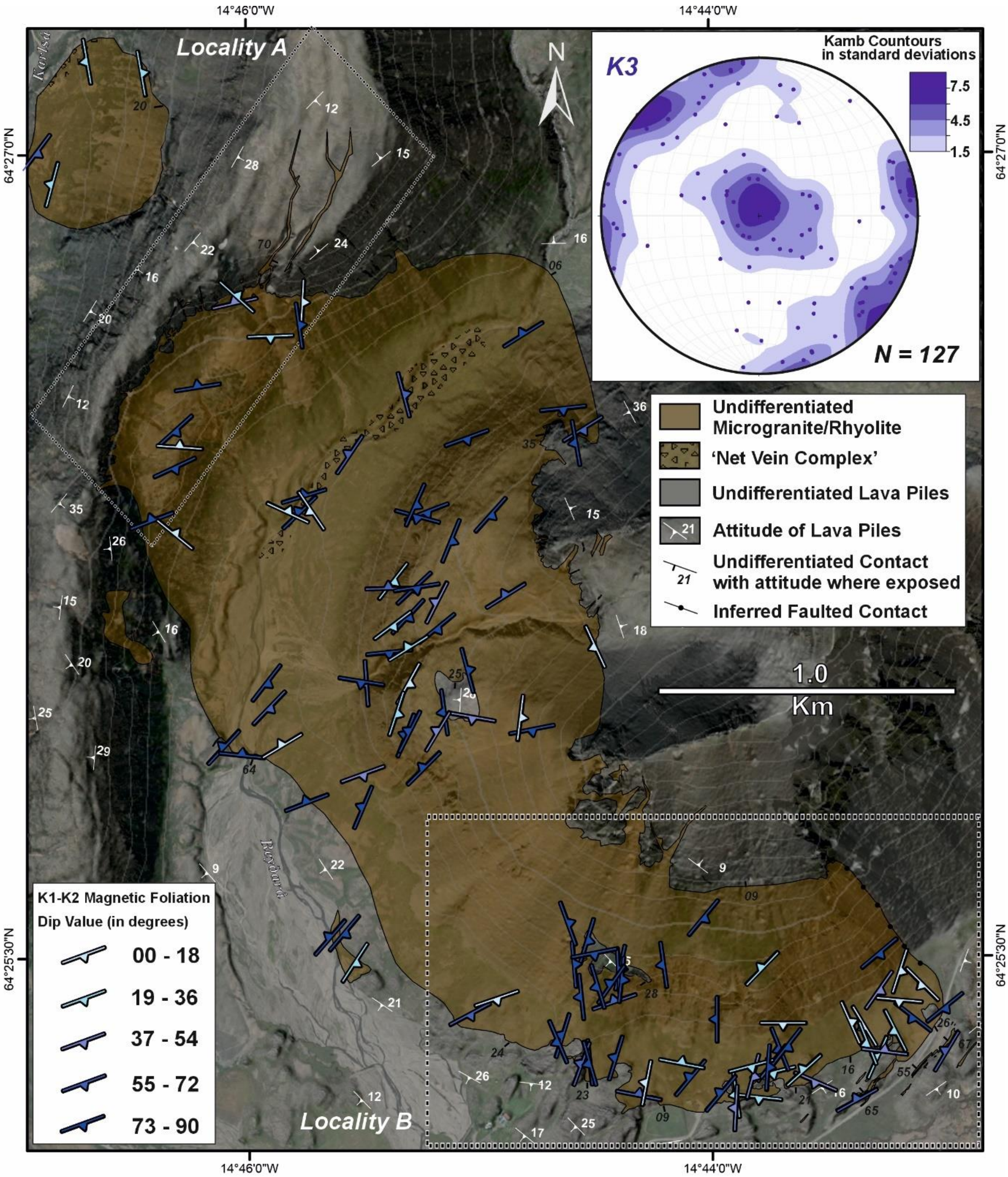

Fig.8: *Map of the Reyðarártindur intrusion plotting K1-K2 (Magnetic Foliation) planes. The degree of dip of the magnetic foliation is colour coded.*

AMS fabrics within steeply inclined sheets

In the NW margin (Locality A; Fig. 2) the AMS fabrics from the two samples directly below the sub-vertical sheet show magnetic lineations that plunge moderately toward the NE, roughly parallel to the nearby inferred contact of the sheet sampled (Fig. 9). The foliation adjacent to the inferred NW margin of the sheet strikes 257º with a moderate dip to the NNW (42º) while, near the inferred SE margin of the sheet, the foliation strikes NW–SE, sub-perpendicular to the strike of the sheet with a moderate dip the NE (30º) (Fig. 9). The T_j values indicate triaxial (-0.026) and near prolate (-0.460) shapes from the northwest and southeast margins respectively in from the northwest to southeast margin respectively while, the P_j value is constant across both sample sites (1.018 – 1.021) (Fig. 9). The resultant vector that is perpendicular to the bisecting line between the two magnetic foliation planes displays an imbricated fabric indicating a sub-vertical magma flow direction that appears to be dip-parallel or slightly dip-oblique attitude the overlying sheet (Fig. 9).

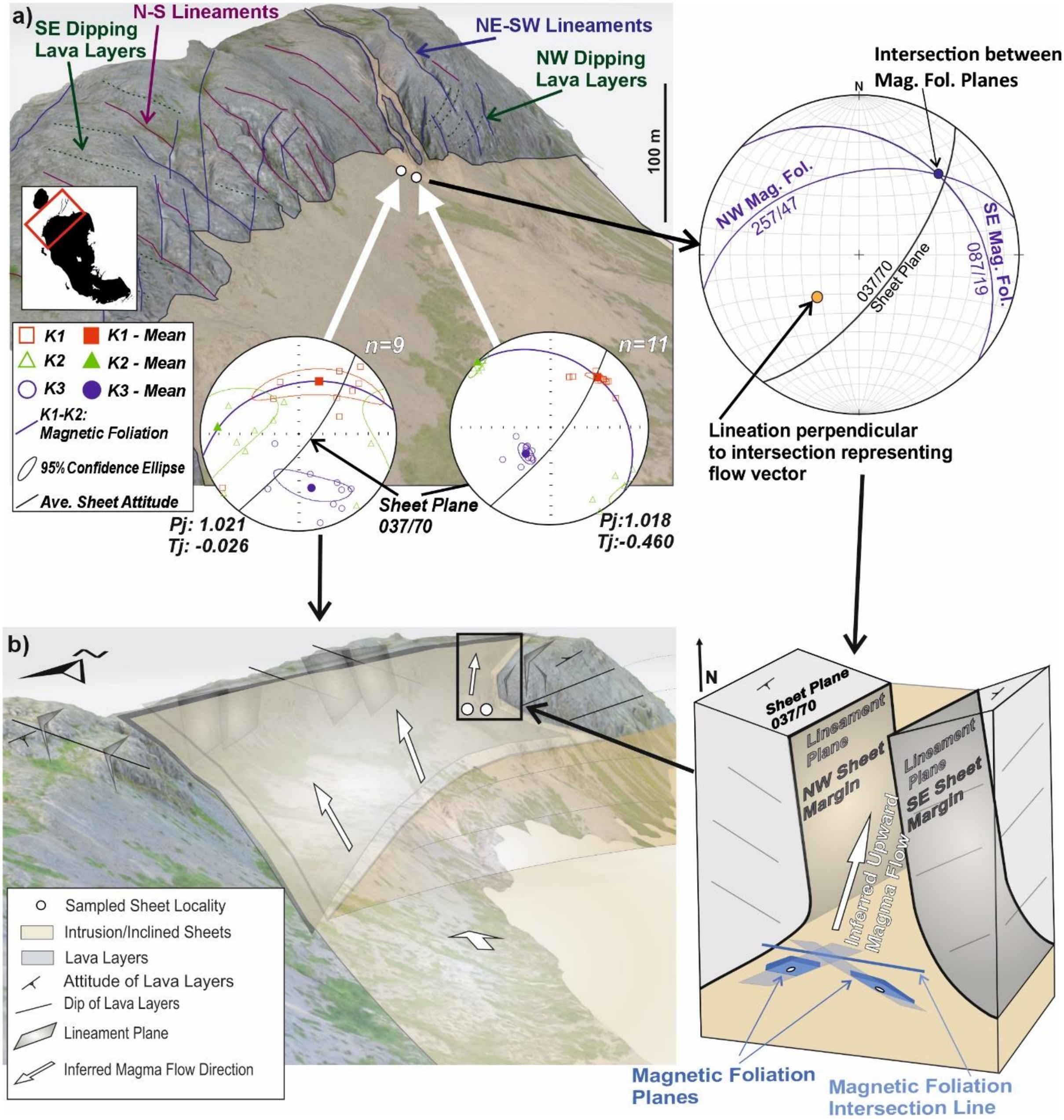

Fig. 9: ***(a)*** *Orthophotograph of Locality A demonstrating the relationship between NNE-SSW fracture sets and inclined magma sheets, highlighting the localities of the AMS samples selected for imbrication directly beneath inclined sheet. Stereographic projections, Pj and T values from each AMS sample site and a projection merging the two samples are also presented, demonstrating their imbrication. (b) 3D projection of Locality A demonstrating a NNE-striking fault controlled upward evacuation of magma on the periphery of the main*

intrusion and a schematic depiction of the magnetic fabric imbrication relative to the overlying vent.

A similar relationship is observed along the southeast margin of the intrusion at Locality B, where block samples were collected from the margins and centre of two steeply inclined granitoid sheets (Fig. 10). Magnetic foliations measured in Sheet 1 strike 216 to 240º with dip values ranging from moderately to steeply inclined (34–86º) to the NW, oblique to the strike of the sheet margin (217/64º, NW contact; 228/67º, SE contact) (Fig. 10). Magnetic foliations in Sheet 2 also show a subparallel relationship with the host rock contact, returning strikes range of 203 to 211º and dip values between 62 and 63º (Fig. 10). The combined field mapping and AMS results therefore show an imbrication geometry exists between the sheet contact and magnetic foliation plane. The trend and plunge of the K_1 and K_2 axes on the magnetic foliation planes vary across both sheets with triaxial to oblate fabrics in Sheet 1 (T_j; 0.131 – 0.522) and more oblate fabrics in Sheet 2 (T_j; 0.424 – 0.669) (Fig. 10). The shape anisotropy (T_j), total degree of anisotropy (P_j) and magnetic susceptibility (K_m) marginally increase in magnetite toward the centre of both sheets (Fig. 10).

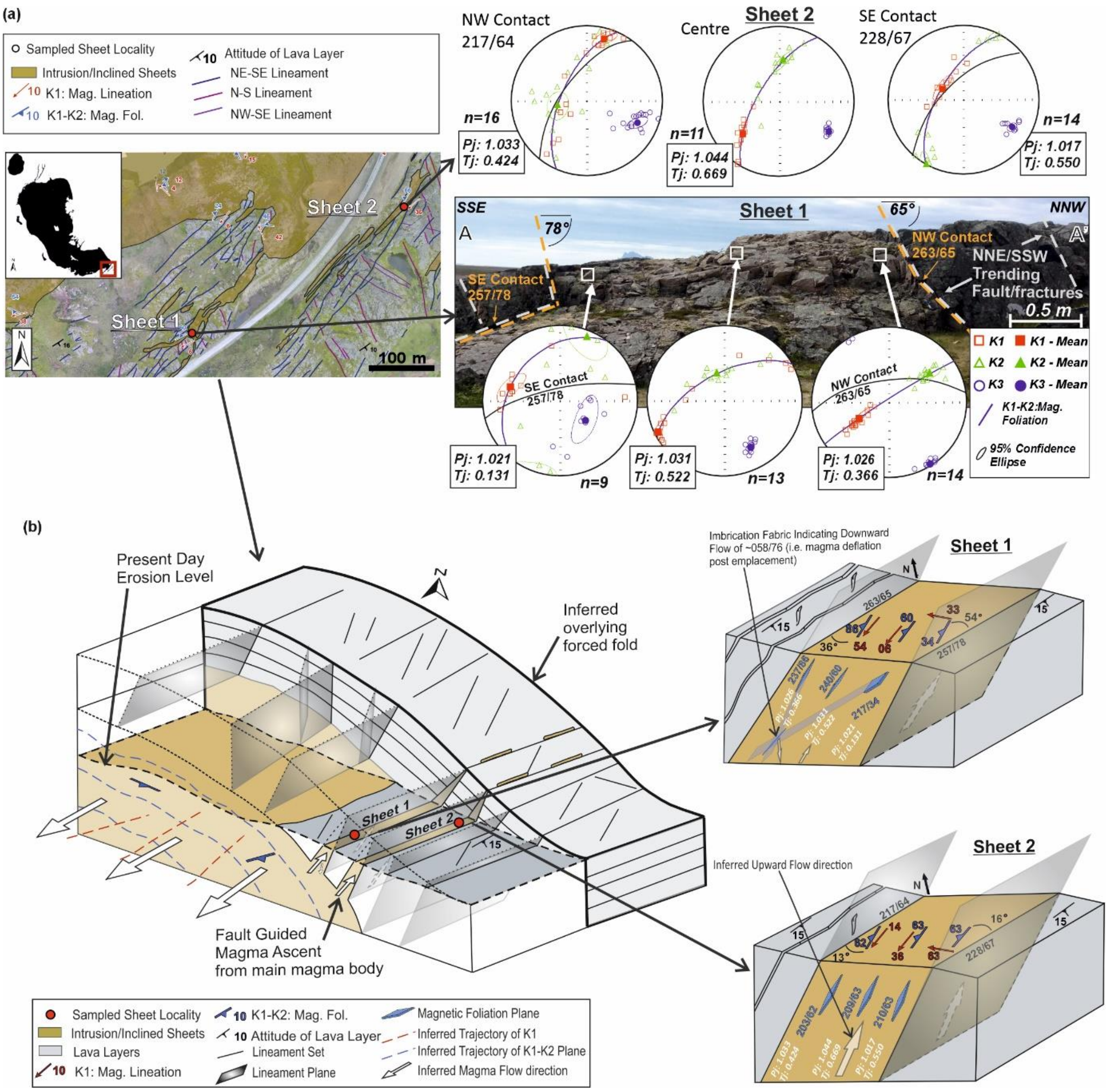

Fig. 10: *(a) Orthophotograph of the SE exposure of the Reyðarártindur intrusion demonstrating relationship between NNE-SSW fracture sets and inclined Sheets 1 and 2 with stereographic projections and Pj and Tj values from AMS sample sites. A photograph of Sheet 1 looking towards the WSW shows the approximate distribution of the samples. (b) Block diagram summarizing the fracture mediated upward redirection of laterally propagating magma at the SE intrusion contact.*

Discussion

The intrusion's contact geometry, host rock structure, and internal rock fabrics preserve three distinct types of data that record the interplay between the structural geology of the host rock and internal magma emplacement processes. Here, we compare these data to assess the interplay between the contemporaneous regional tectonic regime and magma transport in subvolcanic systems.

As with many intrusions, field and petrographic observations do not uniquely require a single emplacement mechanism for the Reyðarártindur intrusion (Figs. 2 and 3). The faulted contact along the intrusion's eastern margin, alongside the dipping host basalt layers towards the intrusion at the NW contact have been interpreted to reflect piecemeal cauldron subsidence as the dominant control on magma emplacement (Rhodes et al., 2021, 2024). However, our interpretation that the S-SE contact describes monoclinal 'forced folding' of the host lavas (Fig. 3) suggests that roof uplift, driven by magma overpressure and facilitated by elastic bending, may also have contributed significantly to creating space for emplacement (e.g., Pollard and Johnson, 1973; Schofield and Totterdell, 2008; Magee et al., 2013; Magee, 2024).

Local collapse of roof or wall-rock blocks may also have occurred, particularly where lava layers dip inward towards the intrusion (e.g. Locality A; Figs 2, 4 and 9). Because the intrusion floor is not exposed, the structural relationship between the lower intrusion margin and the host rock remains uncertain; consequently, laccolithic inflation, piecemeal subsidence, roof uplift, local collapse, and hybrid combinations of these processes must all be considered credible components of the emplacement mechanism.

Magnetic fabrics & magma emplacement processes

Rock magnetic results show pseudosingle to multidomain magnetite is the dominant contributor to magnetic susceptibility in all samples, (Fig. 6), precluding the measured magnetic fabrics being 'inverse' or 'intermediate' in nature (e.g., Potter and Stephenson, 1988; Ferré, 2002). K’ demonstrates that magnetite is the dominant contributor to AMS (Table S3), shown in thin sections as isolated crystals and exsolved/included within hornblende parallel to magmatic state mineral alignment of viscous, mushy magma across the Reyðarártindur intrusion (Fig. 5). Therefore, we infer that the AMS fabrics measure a magmatic state petrofabric across the intrusion. A consistent NNE-SSW trend to magnetic fabrics is measured across the intrusion with most samples featuring a gently plunging lineation and foliation (Figs. 7 and 8). Deviation from this fabric trend is seen at the pluton contacts, where fabrics become steeply inclined, for example at the NW and SE contacts below and within magmatic sheets (Fig. 10), or at some host rock contacts defined by steeply dipping joints (Fig. 8). These changes in petrofabric orientation and inclination to parallel the local contact geometry suggest the magmatic state petrofabric reflects magma emplacement processes rather than a tectonic overprint (e.g., Latimer et al., 2024). Specifically, the sub-horizontal magnetic foliations suggest lateral transport of magma within the Reyðarártindur intrusion was dominant during emplacement, with K_1 defining a sub-horizontal stretching lineation marking magma flow along a NE-SW axis (e.g., Knight and Walker, 1988; Cañón-Tapia and Chávez-Álvarez, 2004; Köpping et al., 2023). Furthermore, the broad change in magnetic foliation strike adjacent to the S and SE margin of the intrusion, where the host lavas describe a NW-striking monocline oriented at a high angle to a prominent NE–SW-directed magnetic lineation, is consistent with predominately SW-directed uniaxial magma transport during emplacement (Fig.11). Detailed examination of steeply inclined fabrics suggests they are imbricated relative to contacts of overlying or host magmatic sheets (Figs 9 and 10). Magnetic imbrications are interpreted to reflect magma transport direction either pointing upwards, due to subvertical magma transport through these structures during magma evacuation, or downwards due to backflow of magma as overpressure wanes following an initial phase of sheet injection (e.g., Knight and Walker, 1988).

In isolation, the magnetic data which are interpreted to reflect a combination of lateral and vertical magma transport processes, are compatible with a range of emplacement mechanisms, including piecemeal construction via floor or roof-block subsidence as proposed by Rhodes et al. (2021, 2024). The absence of an exposed intrusion floor prevents us from excluding such alternatives. However, when the AMS fabrics are integrated with the mapped discontinuities and intrusion-induced deformation geometries in the host rock, a more evolved interpretation emerges whereby emplacement of a predominately NNE-SSW propagating, shallow, laterally propagating body played a major role. The NW–SE-trending monocline is oriented at a high angle to a prominent NE–SW-directed magmatic lineation consistent with predominately SW-directed uniaxial magma transport during laccolithic growth (Fig.11). We therefore propose an emplacement model where laccolithic inflation and magma overpressure dominated the preserved strain pattern within the intrusion, while localised collapse, subsidence, and fracture-controlled evacuation contributed to the final intrusion architecture.

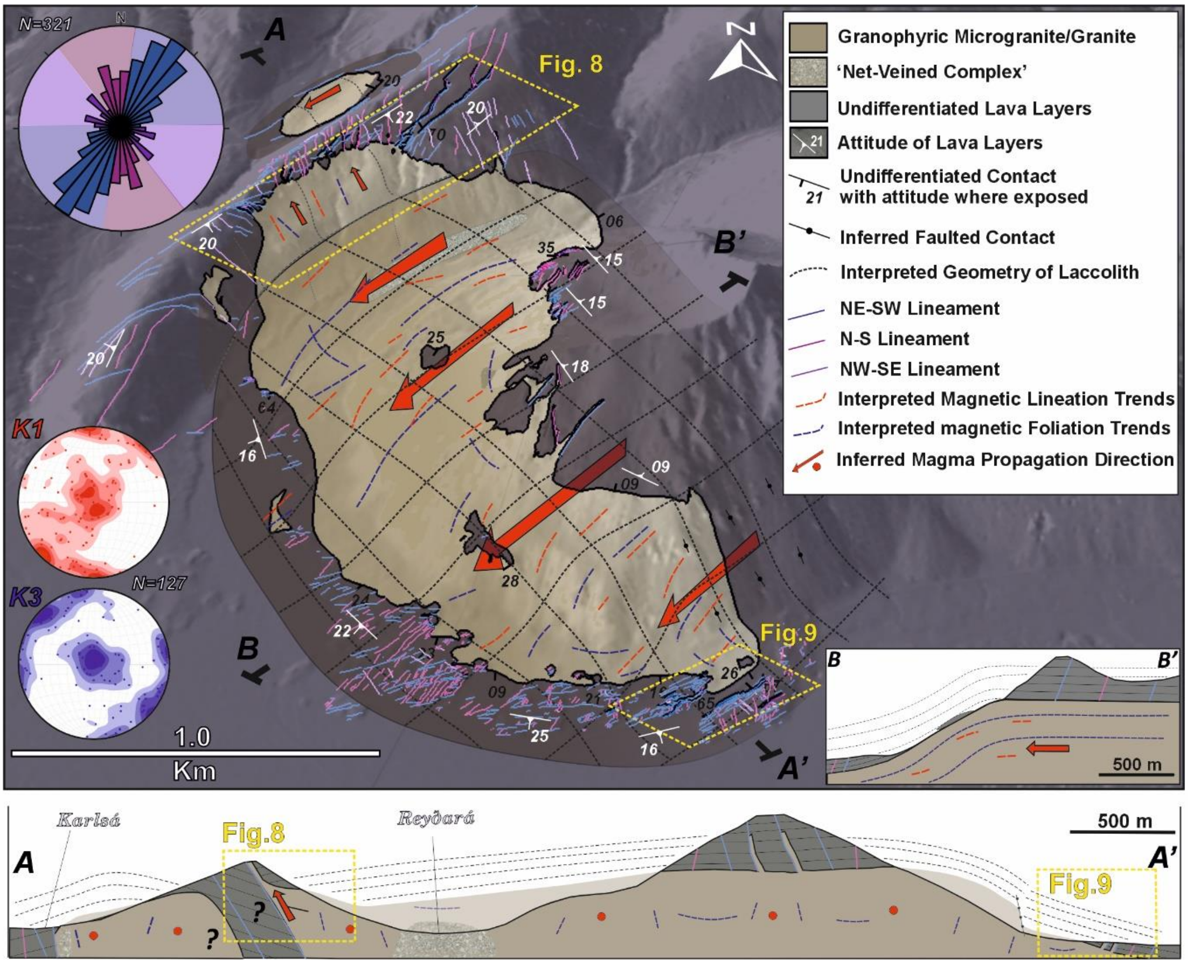

Fig.11: *(a) Schematic of the three-dimensional architecture and emplacement dynamics of the Reyðarártindur intrusion based on the measured magnetic fabrics and observed host rock geometry. Inset are simplified NW-SE (A-A') and SW-NE (B-B') cross-sections of the intrusion.*

The structural aureole and its control on magma evacuation

Integrated field and UAV mapping identify prominent lineament sets within and around the structural aureole of the Reyðarártindur intrusion with three principal trends distinguished: NE-SW (~040–070°), NNW-SSE (~350–020°), and subordinate WNW-ESE lineaments (Fig. 4). Combined field mapping and rock magnetic analysis shows magma intruded along these steeply inclined fractures towards a surface environment (Figs. 9 and 10). The orientation of these lineaments and sheet intrusion sets overlaps with the strike of regional tensile fractures, normal faults, shear faults, and dykes located beyond the structural aureole of the intrusion (cf. Figs 1 and 4). The origin of these lineaments around the Reyðarártindur intrusion may thus not necessarily be singular. Some may have formed or been reactivated by intrusion-induced stresses associated with magma overpressure, host-rock bending, forced folding, roof uplift, and local collapse (Mattsson et al., 2018; Rhodes et al., 2024). Alternatively, or additionally, the observed fault and fracture network could be explained by reactivation of pre-existing fractures derived from the regional tectonic regime (Jacques and Reavy, 1994; DeFrates et al., 2006; Philpotts and Philpotts, 2007). Regardless of their origin, the lineaments local to the Reyðarártindur intrusion, as well as those beyond it's structural aureole, provide insight on the interplay between tectonic deformation and the emplacement of magma during pluton construction, which we discuss here.

Rifting in Iceland often occurs through oblique deformation, expressed as complex en-échelon arrays of conjugate strike-slip and normal faults that trend both parallel and oblique to the rift axis (e.g., Withjack and Jamison, 1986; Tron and Brun, 1991; Fournier and Petit, 2007; Agostini et al., 2009). In such systems, strain is typically accommodated by interconnected fault networks forming shear zones, which can be interpreted using Riedel shear models (Fig. 12) (Dresen et al., 1991; Fossen and Cavalcante, 2017). Riedel shear systems comprise R (synthetic) and R′ (antithetic) shears, X and P faults, and T (tensile) fractures, all oriented at characteristic angles to the principal displacement zone (PDZ) that accommodates the greatest strain (Fig. 12) (Riedel, 1929; Naylor et al., 1986; Sylvester, 1988; Davis et al., 2000; Ahlgren, 2001).

Click or tap here to enter text.

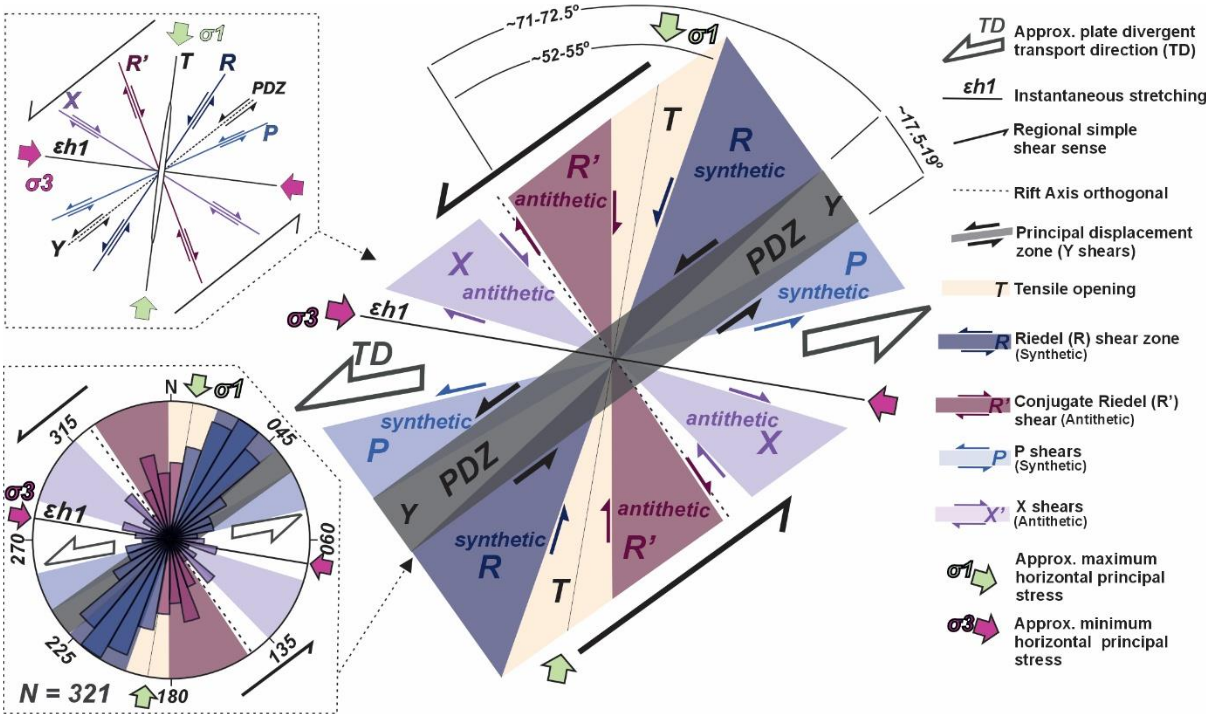

Fig. 12*: Schematic model of a Riedel shear system based on that the observed structural pattern in the host rock surrounding the Reydara intrusion. Colour coding and inset rose plot are based on Fig. 4.*

We note that regional structural data collected from faults, fractures and dykes in southeastern Iceland (Fig. 1) reflect an extensional-to-transtensional stress regime with a net ESE-WNW extensional direction that is perpendicular to the rift zone during the Miocene (e.g., Angelier, 1984; Gudmundsson et al., 2002; Clifton and Kattenhorn, 2006; Keiding et al., 2009). These regional structures, and the lineaments observed around the Reyðarártindur intrusion are compatible with a sinistral Riedel Shear System developed within this broader extensional or transtensional stress field (Figs. 4 and 12).

We interpret that two principal lineament sets recognised around the intrusion, i.e., NE–SW (~040–070°) and NNE–SSW (~350–020°), and those regional structures they parallel, could represent first-order synthetic R-shears and second-order antithetic R′-shears respectively (Figs. 1 and 12). For such a conjugate pair of R- and R’-shears, we would infer a Principal Deformation Zone (PDZ) oriented ~055–085°, with shear angles dependent on the internal friction angle (~31–38°) of the host basalt lavas (Fig. 12). Less abundant WNW–ESE lineaments (~270–315°) may represent X-shears (Fig. 12). Crucially, the geometry of our inferred sinistral Riedel shear system permits formation of NNE–SSW-oriented T-fractures (~000°–015°), consistent with the orientation of the observed regional tensile fractures and dykes (Figs. 1 and 12). We emphasise that this Riedel interpretation is a kinematic model that explains the relative orientation and left-stepping sigmoidal arrangement of the mapped fracture sets (Figs 4, 11 and 12). This interpretation is closely analogous to, and a conceptual comparison to, the findings of Quintella et al. (2026) and the present-day South Iceland Seismic Zone (SISZ), which is defined regionally by a similar W–E sinistral Riedel shear system (Angelier et al., 1982; Einarsson, 1991; Gudmundsson, 2000).

Tectonomagmatic interplay and emplacement of the Reyðarártindur intrusion

Given that the local and regional trends of the different structural lineaments are compatible with a sinistral Riedel shear system, we now explore possible implications for the interplay between magma emplacement and the background tectonic setting. For Reyðarártindur, we note that the AMS foliations and lineations align along a NE–SW axis, consistent with SW-directed magma flow parallel to the dominant R-shear direction of the interpreted Riedel shear system (Figs 11 and 13a). The strong spatial and kinematic correlation between magma flow fabrics and the proposed Riedel shear structures could suggest an interplay between magma transport and ongoing development of a Riedel shear system (Fig 13). Favourably oriented discontinuities, like faults and fractures, within the developing Riedel shear system may locally have helped redirect magma laterally to form the Reyðarártindur intrusion and then its evacuation into sheet-like conduits (Figs. 9 and 10).

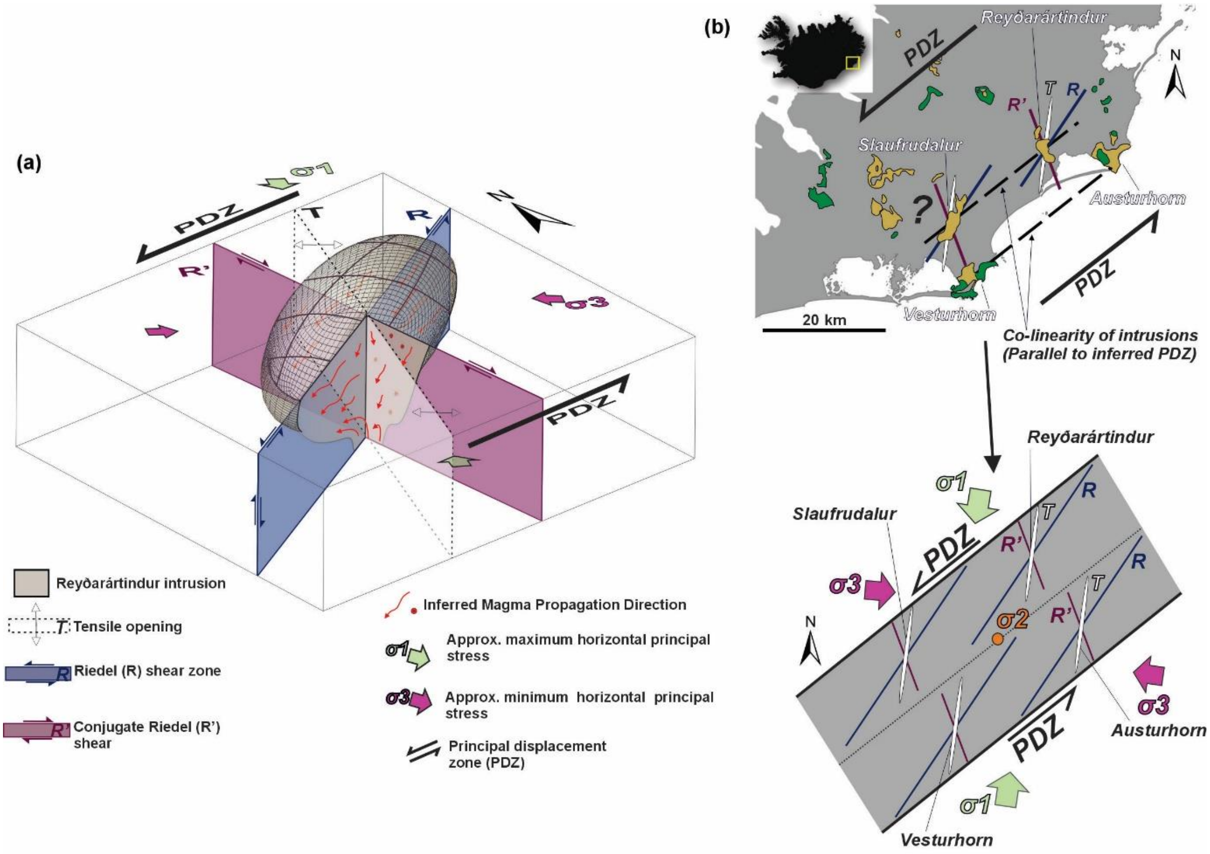

Fig. 13: *(a) Schematic of the proposed relationship between Riedel shear structures and the emplacement of the Reyðarártindur intrusion. (b) Simplified geological map (after Walker, 1974) and schematic depicting the inferred ENE-WSW orientated Neogene transfer zone and potential Neogene rift segment.*

More broadly, an ENE–WSW co-linearity is defined by the Reyðarártindur, Slaufrudalur, Austurhorn, and Vesturhorn intrusions (Fig. 13b). Like our interpretation at Reyðarártindur, the Slaufrudalur intrusion is also interpreted to have been cited along NE-SW conduits (Quintela et al., 2025, 2026), compatible with but not exclusively diagnostic of our inferred Riedel shear system. Regardless, it seems feasible that that the Riedel shear system may have operated/formed on a regional scale whereby ascending intrusive bodies exploit the inferred Principal Displacement Zone (PDZ) of the system resulting in a concentration of intrusions along the ENE-WSW corridor (Fig. 13b). The magmatic state fabrics preserved within these intrusions may further indicate a uniaxial NE-SW orientated axis, consistent with magma transport influenced by Riedel shears within this regional deformation system (Fig. 13b). However, it should be noted that this relationship remains to be tested across the wider intrusive suite.

Our model highlights the interplay between magma overpressure and regional tectonics, in directing magma towards the volcanic edifice. The Reyðarártindur intrusion is shown to preserve a sensitive archive of internal and external-derived stress regimes interacting throughout magma emplacement, with this archive only elucidated when magnetic fabrics are integrated with field and UAV-based fracture mapping. This agrees with the study of the mid-crustal Fanad Pluton by Latimer et al. (2026) who implemented a similar integrated methodology, with their work and our current study highlighting the importance of combing strain records formed throughout magma emplacement to understand processes related to intrusion formation. The feasibility of our interpretive model could be tested by expanding host rock fracture analysis at Slaufrudalur (after Quintela et al., 2026) and constraining magma flow patterns and host rock deformation at the Austurhorn and Vesturhorn intrusions and comparison of fracture kinematics with regional palaeostress datasets.

Conclusions

This study aimed to investigate how regional stress kinematics impact magma transport and eruption pathways in subvolcanic systems, using the Reyðarártindur Intrusion, SE Iceland as a case study. By integrating magnetic fabrics with host rock structural data, we identify a strong spatial and kinematic relationship between AMS fabrics and the surrounding fracture network, with magma transport consistently oriented SW-NE. These fractures form part of a regional NNE–SSW-oriented Riedel shear system, indicating that magma flow was guided by pre-existing tectonic structures rather than developing independently of them. Together, these results support a model in which subvolcanic magma transport at the Reyðarártindur Intrusion was fundamentally controlled by the regional tectonic framework, highlighting the importance of inherited fracture networks in focusing magma emplacement and evacuation pathways. Extending this approach to adjacent intrusions (e.g., Reyðarártindur, Slaufrudalur, Austurhorn, and Vesturhorn) will be key to testing whether this regional fracture system represents a broader structural control on subvolcanic plumbing systems in SE Iceland.

Acknowledgements

This work forms part of a PhD project funded by the School of Earth and Environmental Sciences, University of St Andrews. Fieldwork was generously supported by the Cambridge Arctic Shelf Programme (CASP). We gratefully acknowledge the local communities of southeast Iceland for their hospitality and support during fieldwork. We thank Emma Rhodes, Steffi Burchardt, Tobias Mattsson, and Mike Petronis for constructive discussions that helped shape the development of this study.

References

Acocella, V., Bellier, O., Sandri, L., Sébrier, M., Pramumijoyo, S., 2018. Weak Tectono-Magmatic Relationships along an Obliquely Convergent Plate Boundary: Sumatra, Indonesia. Frontiers in Earth Science 6. https://doi.org/10.3389/feart.2018.00003

Agostini, A., Corti, G., Zeoli, A., Mulugeta, G., 2009. Evolution, pattern, and partitioning of deformation during oblique continental rifting: Inferences from lithospheric-scale centrifuge models. Geochemistry, Geophysics, Geosystems 10. https://doi.org/10.1029/2009GC002676

Ahlgren, S.G., 2001. The nucleation and evolution of Riedel shear zones as deformation bands in porous sandstone. Journal of Structural Geology 23, 1203–1214. https://doi.org/10.1016/S0191-8141(00)00183-8

Akimoto, S., 1962. Magnetic properties of FeO-Fe2O3-TiO2 system as a basis of rock magnetism. Proceedings on the International Conference on Magnetism and Crystallography 17, 706–710.

Alfaro, R., Brandsdóttir, B., Rowlands, D.P., White, R.S., Gudmundsson, M.T., 2007. Structure of the Grímsvötn central volcano under the Vatnajökull icecap, Iceland. Geophysical Journal International 168, 863–876. https://doi.org/10.1111/j.1365-246X.2006.03238.x

Anastasio, D.J., Kodama, K.P., Parés, J.M., Hinnov, L.A., Idleman, B.D., 2021. Internal and External Modulation of Folding Rates With 10^4 to 10^5 Year Time Resolutions From Growth Strata, Pico del Aguila, Spain. Geochemistry, Geophysics, Geosystems 22. https://doi.org/10.1029/2021GC009828

Angelier, J., 1984. Tectonic analysis of fault slip data sets. Journal of Geophysical Research: Solid Earth 89, 5835–5848. https://doi.org/10.1029/JB089iB07p05835

Angelier, J., Tarantola, A., Valette, B., Manoussis, S., 1982. Inversion of field data in fault tectonics to obtain the regional stress ? I. Single phase fault populations: a new method of computing the stress tensor. Geophysical Journal International 69, 607–621. https://doi.org/10.1111/j.1365-246X.1982.tb02766.x

Archanjo, C.J., Bouchez, J.-L., Corsini, M., Vauchez, A., 1994. The Pombal granite pluton: Magnetic fabric, emplacement and relationships with the Brasiliano strike-slip setting of NE Brazil (Paraiba State). Journal of Structural Geology 16, 323–335. https://doi.org/10.1016/0191-8141(94)90038-8

Bemis, S.P., Micklethwaite, S., Turner, D., James, M.R., Akciz, S., Thiele, S.T., Bangash, H.A., 2014. Ground-based and UAV-Based photogrammetry: A multi-scale, high-resolution mapping tool for structural geology and paleoseismology. Journal of Structural Geology 69, 163–178. https://doi.org/10.1016/j.jsg.2014.10.007

Bergerat, F., Angelier, J., Villemin, T., 1990. Fault systems and stress patterns on emerged oceanic ridges: a case study in Iceland. Tectonophysics 179, 183–197. https://doi.org/10.1016/0040-1951(90)90290-O

Biedermann, A.R., Bender Koch, C., Lorenz, W.E.A., Hirt, A.M., 2014. Low-temperature magnetic anisotropy in micas and chlorite. Tectonophysics 629, 63–74. https://doi.org/10.1016/j.tecto.2014.01.015

Biedermann, A.R., Koch, C.B., Pettke, T., Hirt, A.M., 2015. Magnetic anisotropy in natural amphibole crystals. American Mineralogist 100, 1940–1951. https://doi.org/10.2138/am-2015-5173

Biedermann, A.R., Pettke, T., Angel, R.J., Hirt, A.M., 2016. Anisotropy of magnetic susceptibility in alkali feldspar and plagioclase. Geophysical Journal International 205, 479–489. https://doi.org/10.1093/gji/ggw04209

Blake, D.H., 1966. The Net-Veined Complex of the Austurhorn Intrusion, Southeastern Iceland. The Journal of Geology 74, 891–907. https://doi.org/10.1086/627218

Bodvarsson, G., Walker, G.P.L., 2007. Crustal Drift in Iceland. Geophysical Journal of the Royal Astronomical Society 8, 285–300. https://doi.org/10.1111/j.1365-246X.1964.tb06295.x

Bonali, F.L., Tibaldi, A., Marchese F., Fallati L., Russo E., Corselli, C., Savini, A., 2019. UAV-based surveying in volcano-tectonics: An example from the Iceland rift, Journal of Structural Geology, 121,46-64,

Bonali, F.L., Tibaldi, A., Corti, N., Fallati, L., Russo, E., 2020. Reconstruction of Late Pleistocene-Holocene Deformation through Massive Data Collection at Krafla Rift (NE Iceland) Owing to Drone-Based Structure-from-Motion Photogrammetry. Applied Science, 10, 6759. https://doi.org/10.3390/app10196759

Borradaile, G.J., Jackson, M., 2010. Structural geology, petrofabrics and magnetic fabrics (AMS, AARM, AIRM). Journal of Structural Geology 32, 1519–1551. https://doi.org/10.1016/j.jsg.2009.09.006

Bouchez, J.L., 1997. Granite is Never Isotropic: An Introduction to AMS Studies of Granitic Rocks. In: Bouchez, J.L., Hutton, D.H.W., Stephens, W.E. (Eds.). 95–112. https://doi.org/10.1007/978-94-017-1717-5_6

Brune, S., Kolawole, F., Olive, J.-A., Stamps, D.S., Buck, W.R., Buiter, S.J.H., Furman, T., Shillington, D.J., 2023. Geodynamics of continental rift initiation and evolution. Nature Reviews Earth & Environment 4, 235–253. https://doi.org/10.1038/s43017-023-00391-3

Burchardt, S., Annen, C.J., Kavanagh, J.L., Hilmi Hazim, S., 2022. Developments in the study of volcanic and igneous plumbing systems: outstanding problems and new opportunities. Bulletin of Volcanology 84, 59. https://doi.org/10.1007/s00445-022-01564-6

Burchardt, S., Tanner, D., Krumbholz, M., 2012. The Slaufrudalur pluton, southeast Iceland--An example of shallow magma emplacement by coupled cauldron subsidence and magmatic stoping. Geological Society of America Bulletin 124, 213–227. https://doi.org/10.1130/B30430.1

Burton-Johnson, A., Macpherson, C.G., Muraszko, J.R., Harrison, R.J., Jordan, T.A., 2019. Tectonic strain recorded by magnetic fabrics (AMS) in plutons, including Mt Kinabalu, Borneo: A tool to explore past tectonic regimes and syn-magmatic deformation. Journal of Structural Geology 119, 50–60. https://doi.org/10.1016/j.jsg.2018.11.014

Callot, J.-P., Geoffroy, L., Aubourg, C., Pozzi, J.P., Mege, D., 2001. Magma flow directions of shallow dykes from the East Greenland volcanic margin inferred from magnetic fabric studies. Tectonophysics 335, 313–329. https://doi.org/10.1016/S0040-1951(01)00060-9

Cañón-Tapia, E., Chávez-Álvarez, J., 2004. Theoretical aspects of particle movement in flowing magma: implications for the anisotropy of magnetic susceptibility of dykes. Geological Society, London, Special Publications 238, 227–249. https://doi.org/10.1144/GSL.SP.2004.238.01.15

Cargill, H.K., Hawkes, L., Ledeboer, J.A., 1928. The Major Intrusions of South-Eastern Iceland. Quarterly Journal of the Geological Society of London 84, 505–535. https://doi.org/10.1144/GSL.JGS.1928.084.01-04.19

Clark, D.A., 2014. Magnetic effects of hydrothermal alteration in porphyry copper and iron-oxide copper–gold systems: A review. Tectonophysics 624–625, 46–65. https://doi.org/10.1016/j.tecto.2013.12.011

Clifton, A.E., Kattenhorn, S.A., 2006. Structural architecture of a highly oblique divergent plate boundary segment. Tectonophysics 419, 27–40. https://doi.org/10.1016/j.tecto.2006.03.016

Cloos, H., 1926. Einführung in die tektonische Behandlung magmatischer Erscheinungen (Granittektonik). Das Riesengebirge in Schlesien. Borntraeger, Berlin.

Clough, C.T., Maufe, H.B., Bailey, E.B., 1909. The Cauldron-Subsidence of Glen Coe, and the Associated Igneous Phenomena. Quarterly Journal of the Geological Society of London 65, 611–678. https://doi.org/10.1144/GSL.JGS.1909.065.01-04.35

Cruz, C., Sant'Ovaia, H., McCarthy, W., Noronha, F., 2022. Anisotropy of Out-of-Phase Magnetic Susceptibility: A Non-Standard Approach for Magnetic Subfabrics Determination in Variscan Granites of Iberian Massif. Minerals 12. https://doi.org/10.3390/min12111376

Daly, R.A., 1933. Igneous Rocks and the Depths of the Earth. McGraw-Hill Book Co., Inc., New York and London.

Daly, R.A., 1903. The geology of Ascutney Mountain, Vermont. https://doi.org/10.3133/b209

Davis, G.H., Bump, A.P., García, P.E., Ahlgren, S.G., 2000. Conjugate Riedel deformation band shear zones. Journal of Structural Geology 22, 169–190.

Day, R., Fuller, M., Schmidt, V.A., 1977. Hysteresis properties of titanomagnetites: Grain-size and compositional dependence. Physics of the Earth and Planetary Interiors 13, 260–267. https://doi.org/10.1016/0031-9201(77)90108-X

DeFrates, J., Malone, D.H., Craddock, J.P., 2006. Anisotropy of magnetic susceptibility (AMS) analysis of basalt dikes at Cathedral Cliffs, WY: implications for Heart Mountain faulting. Journal of Structural Geology 28, 9–18. https://doi.org/10.1016/j.jsg.2005.09.002

Dresen, G., Gwildis, U., Kluegel, Th., 1991. Numerical and analogue modelling of normal fault geometry. Geological Society, London, Special Publications 56, 207–217. https://doi.org/10.1144/GSL.SP.1991.056.01.14

Dunlop, D., Özdemir, O., 1997. Rock Magnetism: Fundamentals and frontiers, 1st ed. Cambridge University Press, Cambridge.

Einarsson, P., 1991. Earthquakes and present-day tectonism in Iceland. Tectonophysics 189, 261–279. https://doi.org/10.1016/0040-1951(91)90501-I

Eriksson, P.I., Riishuus, M.S., Sigmundsson, F., Elming, S.-Å., 2011. Magma flow directions inferred from field evidence and magnetic fabric studies of the Streitishvarf composite dike in east Iceland. Journal of Volcanology and Geothermal Research 206, 30–45. https://doi.org/10.1016/j.jvolgeores.2011.05.009

Ferré, E.C., 2002. Theoretical models of intermediate and inverse AMS fabrics. Geophysical Research Letters 29, 31-1-31–4. https://doi.org/10.1029/2001GL014367

Fossen, H., Cavalcante, G.C.G., 2017. Shear zones – A review. Earth-Science Reviews 171, 434–455. https://doi.org/10.1016/j.earscirev.2017.05.002

Fournier, M., Petit, C., 2007. Oblique rifting at oceanic ridges: Relationship between spreading and stretching directions from earthquake focal mechanisms. Journal of Structural Geology 29, 201–208. https://doi.org/10.1016/j.jsg.2006.07.017

Furman, T., Meyer, P.S., Frey, F., 1992. Evolution of Icelandic central volcanoes: evidence from the Austurhorn intrusion, southeastern Iceland. Bulletin of Volcanology 55, 45–62. https://doi.org/10.1007/BF00301119

Galland, O., Burchardt, S., Hallot, E., Mourgues, R., Bulois, C., 2014. Dynamics of dikes versus cone sheets in volcanic systems. Journal of Geophysical Research: Solid Earth 119, 6178–6192. https://doi.org/10.1002/2014JB011059

Geoffroy, L., Callot, J.P., Aubourg, C., Moreira, M., 2002. Magnetic and plagioclase linear fabric discrepancy in dykes: a new way to define the flow vector using magnetic foliation. Terra Nova 14, 183–190. https://doi.org/10.1046/j.1365-3121.2002.00412.x

Getzlaff, M., 2008. Fundamentals of Magnetism. Springer Berlin Heidelberg, Berlin, Heidelberg. https://doi.org/10.1007/978-3-540-31152-2

Gudmundsson, A., 2011. Deflection of dykes into sills at discontinuities and magma-chamber formation. Tectonophysics 500, 50–64. https://doi.org/10.1016/j.tecto.2009.10.015

Gudmundsson, A., 2000. Dynamics of Volcanic Systems in Iceland: Example of Tectonism and Volcanism at Juxtaposed Hot Spot and Mid-Ocean Ridge Systems. Annual Review of Earth and Planetary Sciences 28, 107–140. https://doi.org/10.1146/annurev.earth.28.1.107

Gudmundsson, A., 1995. Infrastructure and mechanics of volcanic systems in Iceland. Journal of Volcanology and Geothermal Research 64, 1–22. https://doi.org/10.1016/0377-0273(95)92782-Q

Gudmundsson, A., Fjeldskaar, I., Brenner, S.L., 2002. Propagation pathways and fluid transport of hydrofractures in jointed and layered rocks in geothermal fields. Journal of Volcanology and Geothermal Research 116, 257–278. https://doi.org/10.1016/S0377-0273(02)00225-1

Hjartardóttir, Á.R., Einarsson, P., Bramham, E., Wright, T.J., 2012. The Krafla fissure swarm, Iceland, and its formation by rifting events. Bulletin of Volcanology 74, 2139–2153. https://doi.org/10.1007/s00445-012-0659-0

Hopkinson, J., 1890. Magnetism and Recalescence. Proceedings of the Royal Society of London 48, 442–446.

Hrouda, F., Jelínek, V., Zapletal, K., 1997. Refined technique for susceptibility resolution into ferromagnetic and paramagnetic components based on susceptibility temperature-variation measurement. Geophysical Journal International 129, 715–719. https://doi.org/10.1111/j.1365-246X.1997.tb04506.x

Hutton, D.H.W., 1988. Granite emplacement mechanisms and tectonic controls: Inferences from deformation studies. Transactions of the Royal Society of Edinburgh: Earth Sciences 79, 245–255. https://doi.org/10.1017/S0263593300014255

Hutton, D.H.W., 1982. A tectonic model for the emplacement of the Main Donegal Granite, NW Ireland. Journal of the Geological Society. London 139, 615–631.

Jacques, J.M., Reavy, R.J., 1994. Caledonian plutonism and major lineaments in the SW Scottish Highlands. Journal of the Geological Society, London 151, 955–964.

Jelinek, V., 1981. Characterization of the magnetic fabric of rocks. Tectonophysics 79, T63–T67.

Jelinek, V., 1978. Statistical processing of anisotropy of magnetic susceptibility measured on groups of specimens. Studia Geophysica et Geodaetica Volume 22, 50–62.

Jones, E., McCarthy, W., Magee, C., Mattsson, T., Piazolo, S., Hutchison, W., Humphreys, M.C.S., 2025. Igneous layering and magma dynamics in alkaline intrusions: textural evidence for gravitational settling and compaction within cumulates. Journal of the Geological Society 182. https://doi.org/10.1144/jgs2024-181

Just, J., Kontny, A., Wall, H. DE, Hirt, A.M., Martin-Hernandez, F., 2004. Development of magnetic fabrics during hydrothermal alteration in the Soultz-sous-Forêts granite from the EPS-1 borehole, Upper Rhine Graben. Geological Society, London, Special Publications 238, 509–526. https://doi.org/10.1144/GSL.SP.2004.238.01.26

Kavanagh, J.L., 2018. Mechanisms of Magma Transport in the Upper Crust—Dyking. Volcanic and Igneous Plumbing Systems. Elsevier, 55–88. https://doi.org/10.1016/B978-0-12-809749-6.00003-0

Keiding, M., Lund, B., Árnadóttir, T., 2009. Earthquakes, stress, and strain along an obliquely divergent plate boundary: Reykjanes Peninsula, southwest Iceland. Journal of Geophysical Research: Solid Earth 114. https://doi.org/10.1029/2008JB006253

Kirkland, C.L., Alsop, G.I., Prave, A.R., 2008. The brittle evolution of a major strike-slip fault associated with granite emplacement: a case study of the Leannan Fault, NW Ireland. Journal of the Geological Society 165, 341–352. https://doi.org/10.1144/0016-76492007-064

Klausen, M.B., 2006. Geometry and mode of emplacement of dike swarms around the Birnudalstindur igneous centre, SE Iceland. Journal of Volcanology and Geothermal Research 151, 340–356. https://doi.org/10.1016/j.jvolgeores.2005.09.006

Klausen, M.B., 2004. Geometry and mode of emplacement of the Thverartindur cone sheet swarm, SE Iceland. Journal of Volcanology and Geothermal Research 138, 185–204. https://doi.org/10.1016/j.jvolgeores.2004.05.022

Knight, H., Stevenson, C., Maffione, M., McCarthy, W., Burton-Johnson, A., Lawrence, A., 2024. Testing the sensitivity of anisotropy of magnetic susceptibility (AMS) to the regional tectonic strain field in granite plutons: insights from two orogen-scale studies. Tektonika 2.2, 181–208. https://doi.org/10.55575/tektonika2024.2.2.58

Knight, M.D., Walker, G.P.L., 1988. Magma flow directions in dikes of the Koolau Complex, Oahu, determined from magnetic fabric studies. Journal of Geophysical Research: Solid Earth 93, 4301–4319. https://doi.org/10.1029/JB093iB05p04301

Koopmans, L., Gardiner, N.J., St. Pierre, B., Palin, R.M., Musinga, R., Robb, L.J., 2025. Structural controls on lithium mineralization in shear-zone hosted granitic pegmatites of the Zulu pegmatite field, Zimbabwe – implications for exploration. Mineralium Deposita. https://doi.org/10.1007/s00126-025-01371-x

Köpping, J., Cruden, A.R., Magee, C., McCarthy, W., Geissman, J., Holm, D., 2023. Magnetic fabrics reveal three-dimensional flow processes within elongate magma fingers at the margin of the Shonkin Sag laccolith (MT, USA). Journal of Structural Geology 169. https://doi.org/10.1016/j.jsg.2023.104829

Latimer, B., McCarthy, W., Mattsson, T., Reavy, J., 2026a. Intrusions are sensitive, temporally constrained strain archives. Journal of the Geological Society 183. https://doi.org/10.1144/jgs2025-066

Latimer, B., McCarthy, W., Mattsson, T., Reavy, J., 2026b. The Significance of Magnetic Fabrics Preserved in Hydrothermally Altered Rocks. Journal of Geophysical Research: Solid Earth 131. https://doi.org/10.1029/2025JB033102

Latimer, B., McCarthy, W., Mattsson, T., Reavy, J., 2024. Enclaves as mushy magma strain archives: New perspectives on composite magmatic fabrics in plutons. Geosphere 20, 1390–1410. https://doi.org/10.1130/GES02786.1

Lattard, D., Engelmann, R., Kontny, A., Sauerzapf, U., 2006. Curie temperatures of synthetic titanomagnetites in the Fe-Ti-O system: Effects of composition, crystal chemistry, and thermomagnetic methods. Journal of Geophysical Research: Solid Earth 111. https://doi.org/10.1029/2006JB004591

Magee, C., 2024. Fractures and faults across intrusion-induced forced folds: a georesource perspective. Geological Society, London, Special Publications 547, 109–129. https://doi.org/10.1144/SP547-2023-47

Magee, C., Hunt-Stewart, E., Jackson, C.A.L., 2013. Volcano growth mechanisms and the role of sub-volcanic intrusions: Insights from 2D seismic reflection data. Earth and Planetary Science Letters 373, 41–53. https://doi.org/10.1016/j.epsl.2013.04.041

Magee, C., Muirhead, J., Schofield, N., Walker, R.J., Galland, O., Holford, S., Spacapan, J., Jackson, C.A.L., McCarthy, W., 2019. Structural signatures of igneous sheet intrusion propagation. Journal of Structural Geology 125, 148–154. https://doi.org/10.1016/j.jsg.2018.07.010

Magee, C., Stevenson, C.T.E., Ebmeier, S.K., Keir, D., Hammond, J.O.S., Gottsmann, J.H., Whaler, K.A., Schofield, N., Jackson, C.A.-L., Petronis, M.S., O'Driscoll, B., Morgan, J., Cruden, A., Vollgger, S.A., Dering, G., Micklethwaite, S., Jackson, M.D., 2018. Magma Plumbing Systems: A Geophysical Perspective. Journal of Petrology 59, 1217–1251. https://doi.org/10.1093/petrology/egy064

Magee, C., Stevenson, C.T.E., O'Driscoll, B., Petronis, M.S., 2012. Local and regional controls on the lateral emplacement of the Ben Hiant Dolerite intrusion, Ardnamurchan (NW Scotland). Journal of Structural Geology 39, 66–82. https://doi.org/10.1016/j.jsg.2012.03.005

Marti, A., Folch, A., Costa, A., Engwell, S., 2016. Reconstructing the plinian and co-ignimbrite sources of large volcanic eruptions: A novel approach for the Campanian Ignimbrite. Scientific Reports 6, 21220. https://doi.org/10.1038/srep21220

Marzec, L., 1927. Les plis diapirs et le diapirisme en general. C.R. Seances Inst. Geol. Roumanie 6, 226–270.

Mattsson, T., Burchardt, S., Almqvist, B.S.G., Ronchin, E., 2018. Syn-emplacement Fracturing in the Sandfell Laccolith, Eastern Iceland—Implications for Rhyolite

Intrusion Growth and Volcanic Hazards. Frontiers in Earth Science 6. https://doi.org/10.3389/feart.2018.00005

Mattsson, T., McCarthy, W., Schmiedel, T., 2024. Transport of Magma in Granitic Mush Systems; an Example From the Götemar Pluton, Sweden. Geochemistry, Geophysics, Geosystems 25. https://doi.org/10.1029/2023GC011061

McCarthy, W., Petronis, M.S., Reavy, R.J., Stevenson, C.T., 2015. Distinguishing diapirs from inflated plutons: an integrated rock magnetic fabric and structural study on the Roundstone Pluton, western Ireland. Journal of the Geological Society 172, 550–565. https://doi.org/10.1144/jgs2014-067

Memeti, V., Paterson, S.R., Mundil, R., 2022. Coupled magmatic and host rock processes during the initiation of the Tuolumne Intrusive Complex, Sierra Nevada, California, USA: A transition from ephemeral sheets to long-lived, active magma mushes. GSA Bulletin 134, 1347–1374. https://doi.org/10.1130/B35871.1

Molina Garza, R.S., Geissman, J.W., Peña Alonso, T., Aranda Gómez, J., Wawrzyniec, T., 2021. Structural Setting, Paleomagnetism, and Magnetic Fabric of Miocene Plutons in a Transpressional Sinistral Shear Zone, Tonalá, Chiapas, Mexico: Evidence of Shortening During Magma Emplacement. Tectonics 40. https://doi.org/10.1029/2020TC006559

Molyneux, S.J., Hutton, D.H.W., 2000. Evidence for significant granite space creation by the ballooning mechanism: The example of the Ardara pluton, Ireland. GSA Bulletin 1543–1558.

Naylor, M.A., Mandl, G., Supesteijn, C.H.K., 1986. Fault geometries in basement-induced wrench faulting under different initial stress states. Journal of Structural Geology 8, 737–752. https://doi.org/10.1016/0191-8141(86)90022-2

O'Driscoll, B., Petronis, M.S., Marks, M.A.W., McCarthy, W.S., Mariani, E., Stevenson, C.T.E., Clay, P.L., Geissman, J.W., 2024. Magnetic Fabrics in Laminated Rocks of the Ilímaussaq Igneous Complex, Southern Greenland. The Canadian Journal of Mineralogy and Petrology 62, 821–846. https://doi.org/10.3749/2400008

O'Driscoll, B., Troll, V.R., Reavy, R.J., Turner, P., 2006. The Great Eucrite intrusion of Ardnamurchan, Scotland: Reevaluating the ring-dike concept. Geology 34, 189. https://doi.org/10.1130/G22294.1

Padilla, A.D.J., 2015. Elemental and isotopic geochemistry of crystal-melt systems: Elucidating the construction and evolution of silicic magmas in the shallow crust, using examples from southeast Iceland and southwest USA. PhD Thesis. Vanderbilt University, Nashville.

Padilla, A.J., Miller, C.F., Carley, T.L., Economos, R.C., Schmitt, A.K., Coble, M.A., Wooden, J.L., Fisher, C.M., Vervoort, J.D., Hanchar, J.M., 2016. Elucidating the magmatic history of the Austurhorn silicic intrusive complex (southeast Iceland) using zircon elemental and isotopic geochemistry and geochronology. Contributions to Mineralogy and Petrology 171, 69. https://doi.org/10.1007/s00410-016-1279-z

Passerini, P., Marcucci, M., Sguazzoni, G., Pecchioni, E., 1997. Longitudinal strike-slip faults in oceanic rifting: a mesostructural study from western to southeastern Iceland. Tectonophysics 269, 65–89. https://doi.org/10.1016/S0040-1951(96)00153-9

Paterson, S., Memeti, V., Mundil, R., Žák, J., 2016. Repeated, multiscale, magmatic erosion and recycling in an upper-crustal pluton: Implications for magma chamber dynamics and magma volume estimates. American Mineralogist 101, 2176–2198. https://doi.org/10.2138/am-2016-5576

Paterson, S.R., Fowler, T.K., Schmidt, K.L., Yoshinobu, A.S., Yuan, E.S., Miller, R.B., 1998. Interpreting magmatic fabric patterns in plutons. Lithos 44, 53–82. https://doi.org/10.1016/S0024-4937(98)00022-X

Paterson, S.R., Vernon, R.H., 1995. Bursting the bubble of ballooning plutons: A return to nested diapirs emplaced by multiple processes. Geological Society of America Bulletin 107, 1356–1380.

Petronis, M.S., O'Driscoll, B., Stevenson, C.T.E., Reavy, R.J., 2012. Controls on emplacement of the Caledonian Ross of Mull Granite, NW Scotland: Anisotropy of magnetic susceptibility and magmatic and regional structures. Bulletin of the Geological Society of America 124, 906–927. https://doi.org/10.1130/B30362.1

Philpotts, A.R., Philpotts, D.E., 2007. Upward and downward flow in a camptonite dike as recorded by deformed vesicles and the anisotropy of magnetic susceptibility (AMS). Journal of Volcanology and Geothermal Research 161, 81–94. https://doi.org/10.1016/j.jvolgeores.2006.11.006

Plateaux, R., Bergerat, F., Béthoux, N., Villemin, T., Gerbault, M., 2012. Implications of fracturing mechanisms and fluid pressure on earthquakes and fault slip data in the east Iceland rift zone. Tectonophysics 581, 19–34. https://doi.org/10.1016/j.tecto.2012.01.013

Pollard, D.D., Johnson, A.M., 1973. Mechanics of growth of some laccolithic intrusions in the Henry mountains, Utah, II. Tectonophysics 18, 311–354. https://doi.org/10.1016/0040-1951(73)90051-6

Potter, D.K., Stephenson, A., 1988. Single-domain particles in rocks and magnetic fabric analysis. Geophysical Research Letters 15, 1097–1100. https://doi.org/10.1029/GL015i010p01097

Quintela, O., Burchardt, S., Mattsson, T., Almqvist, B., Stevenson, C., McCarthy, W., Óskarsson, B. V., Pitcairn, I., Rhodes, E., Witcher, T., Greiner, S.H.M., Latimer, B., 2025. The Magnetic Fingerprint of Pulsed Granite Magma Emplacement and Alteration: Slaufrudalur Pluton, Iceland. Geochemistry, Geophysics, Geosystems 26. https://doi.org/10.1029/2025GC012199

Quintela, O., Burchardt, S., Mattsson, T., Óskarsson, B. V., Pitcairn, I., Stevenson, C.T., Askew, R.A., Gallagher, C.R., 2026. Structural aureoles as proxies for magma emplacement in the brittle crust: Evidence for transtensional pluton formation at Slaufrudalur, Iceland. Journal of Volcanology and Geothermal Research 470, 108506. https://doi.org/10.1016/j.jvolgeores.2025.108506

Ramberg, H., 1970. Model studies in relation to intrusion of plutonic bodies. Mechanism of Igneous Intrusion. Geological Journal Special Issue 261–286.

Reeves, J., Magee, C., Jackson, C.A.-L., 2018. Unravelling intrusion-induced forced fold kinematics and ground deformation using 3D seismic reflection data. Volcanica 1, 1–17. https://doi.org/10.30909/vol.01.01.0117

Rhodes, E., Burchardt, S., Greiner, S.H.M., Mattsson, T., Sigmundsson, F., Schmiedel, T., Barker, A.K., Witcher, T., 2024. Volcanic unrest as seen from the magmatic source: Reyðarártindur pluton, Iceland. Scientific Reports 14. https://doi.org/10.1038/s41598-023-50880-0

Rhodes, E.L., Barker, A.K., Burchardt, S., Hieronymus, C.F., Rousku, S.N., McGarvie, D.W., Mattsson, T., Schmiedel, T., Ronchin, E., Witcher, T., 2021. Rapid Assembly and Eruption of a Shallow Silicic Magma Reservoir, Reyðarártindur Pluton, Southeast Iceland. Geochemistry, Geophysics, Geosystems 22. https://doi.org/10.1029/2021GC009999

Richey, J.E., 1927. The Structural Relations of the Mourne Granites, Northern Ireland. Quarterly Journal of the Geological Society of London 83, 653. https://doi.org/10.1144/GSL.JGS.1927.083.01-05.27

Riedel, W., 1929. Zur Mechanik Geologischer Brucherscheinungen. Centralblatt Für Mineralogie, Geologie Und Paläontologie 8, 354–368.

Rivalta, E., Taisne, B., Bunger, A.P., Katz, R.F., 2015. A review of mechanical models of dike propagation: Schools of thought, results and future directions. Tectonophysics 638, 1–42. https://doi.org/10.1016/j.tecto.2014.10.003

Rochette, P., Aubourg, C., Perrin, M., 1999. Is this magnetic fabric normal? A review and case studies in volcanic formations. Tectonophysics 307, 219–234. https://doi.org/10.1016/S0040-1951(99)00127-4

Rubin, A.M., 1995. Propagation of Magma-Filled Cracks. Annual Review of Earth and Planetary Sciences 23, 287–336. https://doi.org/10.1146/annurev.ea.23.050195.001443

Saemundsson, K., 1980. Geology of the European countries. Dunod ; Distributed by Graham & Trotman.

Schofield, Anthony., Totterdell, J.., 2008. Distribution, timing and origin of magmatism in the Bight and Eucla Basins (GeoCat # 67359), Geoscience Austrailia. Geoscience Australia.

Stevenson, C.T.E., Owens, W.H., Hutton, D.H.W., 2007a. Flow lobes in granite: The determination of magma flow direction in the Trawenagh Bay Granite, northwestern Ireland, using anisotropy of magnetic susceptibility. Bulletin of the Geological Society of America 119, 1368–1386. https://doi.org/10.1130/B25970.1

Stevenson, C.T.E., Owens, W.H., Hutton, D.H.W., Hood, D.N., Meighan, I.G., 2007b. Laccolithic, as opposed to cauldron subsidence, emplacement of the Eastern Mourne pluton, N. Ireland: evidence from anisotropy of magnetic susceptibility. Journal of the Geological Society 164, 99–110. https://doi.org/10.1144/0016076492006-008

Sturkell, E., Einarsson, P., Sigmundsson, F., Geirsson, H., Ólafsson, H., Pedersen, R., de Zeeuw-van Dalfsen, E., Linde, A.T., Sacks, S.I., Stefánsson, R., 2006. Volcano geodesy and magma dynamics in Iceland. Journal of Volcanology and Geothermal Research 150, 14–34. https://doi.org/10.1016/j.jvolgeores.2005.07.010

Sturkell, E., Einarsson, P., Sigmundsson, F., Hreinsdóttir, S., Geirsson, H., 2003. Deformation of Grímsvötn volcano, Iceland: 1998 eruption and subsequent inflation. Geophysical Research Letters 30. https://doi.org/10.1029/2002GL016460

Sylvester, A.G., 1988. Strike-slip faults. GSA Bulletin 100, 1666–1703.

Tarling, D.H., Hrouda, F., 1993. The magnetic anisotropy of rocks. Chapman & Hall.

Tauxe, L., 1998. Paleomagnetic Principles and Practice, 1st ed. Dordrecht: Kluwer Academic Publishers.

Thorarinsson, S.B., Tegner, C., 2009. Magma chamber processes in central volcanic systems of Iceland: constraints from layered gabbro of the Austurhorn intrusive complex. Contributions to Mineralogy and Petrology 158, 223–244. https://doi.org/10.1007/s00410-009-0379-4

Tibaldi, A., 2015. Structure of volcano plumbing systems: A review of multi-parametric effects. Journal of Volcanology and Geothermal Research 298, 85–135. https://doi.org/10.1016/j.jvolgeores.2015.03.023

Torfason, H., 1979. Investigations into the structure of South-Eastern Iceland. PhD Thesis. University of Liverpool, Liverpool.

Tron, V., Brun, J.-P., 1991. Experiments on oblique rifting in brittle-ductile systems. Tectonophysics 188, 71–84. https://doi.org/10.1016/0040-1951(91)90315-J

Twomey, V., 2023. The interplay between deformation and magma transport in Southeast Iceland. PhD. University of St Andrews, St Andrews. https://doi.org/10.17630/sta/318

Twomey, V., McCarthy, W., Magee, C., Latimer, B., 2026. Supplementary Material: Subvolcanic magma pathways in transtensional regimes., Dataset. https://doi.org/10.6084/m9.figshare.32083893

Vernon, R.H., Paterson, S.R., 1993. The Ardara pluton, Ireland: deflating an expanded intrusion. Lithos 31, 17–32.

Verwey, E.J.W., Haayman, P.W., 1941. Electronic conductivity and transition point of magnetite (“Fe3O4”). Physica 8, 979–987. https://doi.org/10.1016/S0031-8914(41)80005-6

Vollgger, S.A., Cruden, A.R., 2016. Mapping folds and fractures in basement and cover rocks using UAV photogrammetry, Cape Liptrap and Cape Paterson, Victoria, Australia. Journal of Structural Geology 85, 168–187. https://doi.org/10.1016/j.jsg.2016.02.012

Walker, G.P.L., 1974. The Structure of Eastern Iceland. Geodynamics of Iceland and the North Atlantic Area. Springer Netherlands, Dordrecht, 177–188. https://doi.org/10.1007/978-94-010-2271-2_12

Walker, G.P.L., 1960. Zeolite Zones and Dike Distribution in Relation to the Structure of the Basalts of Eastern Iceland. The Journal of Geology 68, 515–528.

Weidendorfer, D., Mattsson, H.B., Ulmer, P., 2014. Dynamics of Magma Mixing in Partially Crystallized Magma Chambers: Textural and Petrological Constraints from the Basal

Complex of the Austurhorn Intrusion (SE Iceland). Journal of Petrology 55, 1865–1903. https://doi.org/10.1093/petrology/egu044

Weismüller, C., Urai, J.L., Kettermann, M., von Hagke, C., Reicherter, K., 2019. Structure of massively dilatant faults in Iceland: lessons learned from high-resolution unmanned aerial vehicle data. Solid Earth 10, 1757–1784. https://doi.org/10.5194/se-10-1757-2019

Williams, K.M., Urbani, S., Mariani, E., Biggin, A., Wheeler, J., Kavanagh, J.L., 2025. Unravelling the complex record of magma flow and solidification in sills. Journal of the Geological Society 182. https://doi.org/10.1144/jgs2024-120

Witcher, T., Burchardt, S., Mattsson, T., Heap, M.J., McCarthy, W., 2024. Development of permeable networks by viscous-brittle deformation in a shallow rhyolite intrusion. Part 1: Field evidence. Journal of Volcanology and Geothermal Research 454. https://doi.org/10.1016/j.jvolgeores.2024.108166

Withjack, M.O., Jamison, W.R., 1986. Deformation produced by oblique rifting. Tectonophysics 126, 99–124. https://doi.org/10.1016/0040-1951(86)90222-2

Žák, J., Paterson, S.R., Memeti, V., 2007. Four magmatic fabrics in the Tuolumne batholith, central Sierra Nevada, California (USA): Implications for interpreting fabric patterns in plutons and evolution of magma chambers in the upper crust. Bulletin of the Geological Society of America 119, 184–201. https://doi.org/10.1130/B25773.1